International Journal of Thermofluids 29 (2025) 101331

Contents lists available at ScienceDirect

International Journal of Thermofluids

journal homepage: www.elsevier.com/locate/ijtf

An optimized cubic B-spline algorithm for high-precision approximation of nonlinear transport phenomena

Rabia Noureen [a,b], Muhammad Kashif Iqbal [a], Maryam Asgir [c], Bandar Almohsen [d], Muhammad Azeem [e], Husam A. Neamah [f,g,h,i,*]

[a] Department of Mathematics, Government College University, Faisalabad 38000, Pakistan
[b] Department of Mathematics, Government College Women University Faisalabad, Pakistan
[c] Department of Mathematics, Government College University, Lahore, Pakistan
[d] Department of Mathematics, King Saud University, Riyadh, Saudi Arabia
[e] Department of Mathematics, Riphah International University, Lahore, Pakistan
[f] Department of Electrical Engineering and Mechatronics, Faculty of Engineering, University of Debrecen, Ótemetö Utca 2-4, 4028 Debrecen, Hungary
[g] Technical Engineering College, Al-Ayen University, Thi-Qar, 4028, Iraq
[h] Department of Business Management, Al-imam University College, Balad, Iraq
[i] College of Engineering, National University of Science and Technology, Dhi-Qar, 64001, Iraq

ARTICLE INFO

Keywords:
Nonlinear gas dynamics equation
Finite difference formulation
Extended cubic B-spline functions
Stability
Convergence analysis

ABSTRACT

This study aims to investigate a numerical scheme based on etics, Riphah Internatxtended cubic B-spline functions for solving the nonlinear gas dynamics equation, which plays a crucial role in the study of physical phenomena such as explosions, combustion, detonation and condensation within moving flows. The standard finite difference formulation has been employed to approximate the time derivative, while the solution curve in spatial direction is interpolated using extended cubic B-spline functions. A comprehensive stability analysis of the scheme is provided to ensure that errors do not propagate over time. Additionally, a convergence analysis for cubic B-spline interpolation is conducted to assess the accuracy of the solution. The effectiveness and efficiency of the proposed method are tested through numerical simulations. The findings indicate that the proposed technique provides better error estimates compared to other methods discussed in the literature. The straightforward algorithm, high accuracy and minimal computational efforts are the major advantages of this approach. Therefore, the proposed method may serve as a promising and efficient alternative for the numerical solution of nonlinear partial differential equations.

1. Introduction

The study of motion and energy transfer in compressible media has a rich history and is fundamental to numerous scientific and engineering applications, ranging from aerospace to energy systems. This discipline explores the fundamental principles that laid the groundwork for understanding the behavior of gases, including the equations of state, conservation laws and the concept of compressible flow. Gas dynamics, a crucial branch of fluid mechanics, plays a pivotal role in numerous scientific, engineering and technological domains.

Gas dynamics serves as the foundation for aerospace engineering, facilitating the design, analysis and optimization of aircraft and spacecraft propulsion systems. By examining the aerodynamics of airfoils, wings and bodies, gas dynamics contributes to improvements in lift and reductions in drag. It also supports the development of efficient jet engines, rockets and other propulsion technologies.

Understanding combustion dynamics is critical for efficient energy conversion and environmental sustainability. Principles of gas dynamics are applied to investigate combustion phenomena, including flame propagation, detonations and fuel injection dynamics in engines and power generation systems.

Moreover, gas dynamics provides valuable insights into atmospheric motions, weather phenomena and climate modeling. It helps to analyze the behavior of air masses, the formation of clouds, the development of storms and the study of atmospheric waves and their effects on weather patterns.

Additionally, gas dynamics principles are employed in environmental engineering, pollution dispersion modeling and various industrial

* Corresponding author at: Department of Electrical Engineering and Mechatronics, Faculty of Engineering, University of Debrecen, Ótemetö Utca 2-4, 4028 Debrecen, Hungary.
E-mail addresses: rabianoureen26@gcuf.edu.pk, rabianoureen@gcwuf.edu.pk (R. Noureen), kashifiqbal@gcuf.edu.pk (M.K. Iqbal), maryam.asghar90@gmail.com (M. Asgir), balmohsen@ksu.edu.sa (B. Almohsen), azeemali7009@gmail.com (M. Azeem), husam@eng.unideb.hu (H.A. Neamah).

https://doi.org/10.1016/j.ijft.2025.101331
Received 23 February 2025; Received in revised form 12 May 2025; Accepted 10 July 2025
Available online 24 July 2025

processes. It aids in analyzing pollutant transport, designing ventilation systems, optimizing gas pipeline design and enhancing fluid flow in industrial applications.

The equations of gas dynamics [1] represent mathematical representations rooted in the governing principles of conservation laws, such as the conservation of mass, momentum and energy. Within the realm of ideal gas dynamics, nonlinear equations facilitate the modeling of three distinct types of waves: shock fronts, rarefactions and contact discontinuities.

This work deals with the following class of nonlinear gas dynamics equations as

$$\frac{\partial v(\zeta^*,t^*)}{\partial t^*}+\alpha v(\zeta^*,t^*)\frac{\partial v(\zeta^*,t^*)}{\partial \zeta^*}-\beta v(\zeta^*,t^*)(1-v(\zeta^*,t^*)) = f(\zeta^*,t^*), \quad \dot{a}\le\zeta^*\le\dot{b}, \quad t^*\in[0,\mathcal{T}], \tag{1.1}$$

supplemented with the following stipulations

$$v(\zeta^*,0)=\phi(\zeta^*), \tag{1.2}$$

$$v(\dot{a},t^*)=\psi_1(t^*), \quad v(\dot{b},t^*)=\psi_2(t^*), \tag{1.3}$$

where $v(\zeta^*,t^*)$ typically represents the velocity of the gas at position ζ^* and time t^*, α and β are the coefficients of convection and reaction, respectively, and $f(\zeta^*,t^*)$ represents the source term. For $\alpha=1$ and $\beta=1$, Eq. (1.1) reduces to the classical non-homogeneous nonlinear gas dynamics equation.

The quest for exact, analytical and numerical solutions to gas dynamics equations has long attracted significant attention in mathematical physics, fluid motion and in modeling nonlinear wave phenomena. Golubyatnikov and Ukrainskii [2] investigated an exact solution using power series expansions depending on a special time variable, the form of which characterizes the particular class of motion within one-dimensional time-dependent gas dynamics. Another exact solution addressing gas flow in a tube with a piston, governed by the equations of time-dependent, one-dimensional gas dynamics with plane waves, was provided by Ukrainskii [3]. A series solution for the nonlinear gas dynamic equation has also been presented using the Aboodh transform and modified homotopy perturbation method, as reported in [4]. A semi-analytical implicit direct time integration technique for addressing a one-dimensional gas dynamic problem formulated in Lagrangian coordinates was developed in [5]. Meanwhile, the authors in [6] examined the solution of the model problem employing a semi-analytical approach known as the homotopy analysis method. Yindoula et al. [7] employed the Laplace variational iteration method to derive the analytical solution for the nonlinear equation of gas dynamics. This method was based on the determination of the Lagrange multiplier. Edeki et al. [8] investigated an analytical solution to the nonhomogeneous gas dynamic model using the successive approximation method. Kasumo [9] examined the classical gas dynamics equation through a semi-analytical iterative approach.

Numerical solutions are preferred over analytical ones because they offer greater flexibility in handling complicated geometries, variable coefficients and diverse boundary conditions that analytical methods cannot easily handle. Moreover, an advancement in computational power allows these methods to produce highly accurate results, making them more efficient and favorable for practical applications.

Splines are often preferred over other numerical methods because they provide a continuous, smooth, piecewise approximation to the data along with continuous derivatives up to a certain degree. Because splines work piecewise, adjusting the approximation within any interval does not affect the entire region. This property is highly beneficial for handling sharp or irregular changes in the data. Additionally, these functions, characterized by their flexibility, smoothness and compact support, possess remarkable properties that make them well-suited for a wide range of applications. One significant application lies in computer-aided geometric design (CAGD), where B-spline curves and surfaces play a pivotal role in representing complex shapes and facilitating smooth parametrization. B-splines serve as a foundation for constructing efficient and accurate numerical algorithms for solving differential equations, optimization problems, numerical integration, image reconstruction, data compression, feature extraction, deep learning, machine learning and computer vision. The application of B-spline functions demonstrates the immense potential of these functions in tackling challenging problems across various disciplines, paving the way for further advancements in mathematical analysis and computational science.

In recent years, B-splines have found extensive application in trajectory planning and control systems, particularly within the fields of mechatronics and robotics. For instance, [10,11] employed B-splines to enhance UAV navigation, improving real-time adaptability in cluttered environments. Additional studies have highlighted the potential of B-splines in designing path planners for the safe navigation of mobile robots [12], as well as in modeling the nonlinear dynamics of flexible robotic arms to achieve greater precision and control [13,14].

Ali and Senu [15] proposed approximate solutions for third-order linear Volterra and Fredholm integro-differential equations using cubic B-spline functions combined with the Gauss–Legendre quadrature formula. In [16], the authors developed a numerical solution for a linear two-point boundary value problem by employing a modified cubic B-spline basis with the collocation method. Yousafzai et al. [17] presented a numerical approach using cubic B-spline functions to approximate the solution of the nonlinear foam-drainage model. Additionally, Latif et al. [18] investigated a linear two-point boundary value problem using a novel cubic B-spline approximation technique.

Numerical techniques employed for solving the nonlinear gas dynamics equation encompass the variational iteration method, as demonstrated by Prakash and Kumar [19], the Laplace–Carson transform combined with the homotopy perturbation method, as presented by Nadeem and Ali [20], the fourth-order Runge-Kutta (RK-4) method, examined in [6], the reproducing kernel Hilbert space method, discussed by Akgul et al. [21], the modified new iterative method, demonstrated by Iyanda [22], the collocation method with Muntz–Legendre polynomials, introduced by Jebreen and Cattani [23] and the conformable finite-difference approach, proposed in [24].

While the latest studies have extended the gas dynamics equation to fractional time derivatives to account for memory effects [25–27], the classical integer-order form remains fundamental in modeling many practical systems. Furthermore, efficient numerical methods for the nonlinear integer-order case are still an active area of research, especially for complex boundary or initial conditions.

Recent developments in the study of computational solutions to the gas dynamics equation have served as the primary motivation for the current research. This article aims to address the nonlinear gas dynamics equation by combining the finite difference scheme with the extended cubic B-spline collocation method. The extended cubic B-spline functions, which encompass a free parameter enabling fine-tuning of the solution curve, serve as a generalization of cubic B-spline functions. To discretize the time derivative, the standard finite difference scheme is utilized while the extended cubic B-spline functions are employed to interpolate the solution curve along the spatial grid. The proposed method is analyzed for stability and uniform convergence. The approximate solutions and the numerical errors are presented and compared with analytical solutions and the results available in the literature.

The manuscript is organized as follows: Section 2 provides a concise overview of the numerical method employed in the study. In Section 3, the stability analysis of the proposed algorithm is investigated. Section 4 presents a detailed description of the theoretical convergence of the method. The computational results obtained from the implementation of the method are presented and analyzed in Section 5. Finally, in Section 6, concluding remarks summarizing the key findings and implications of the study are presented.

2. Description of numerical approach

In this section, the derivation of the numerical scheme is presented.

2.1. Temporal discretization

Consider the temporal domain, denoted as $[0, \mathcal{T}]$, which is partitioned into $\mathcal{J}$ subintervals represented by $[t_{\mathrm{j}}^*, t_{\mathrm{j+1}}^*]$, where $\mathrm{j} = 0, 1, 2, \ldots, \mathcal{J}$. Here, t_{j}^* corresponds to $t_{\mathrm{j}}^* = t_0^* + \mathrm{j}\Delta t^*$ where $\Delta t^* = \frac{\mathcal{T}}{\mathcal{J}}$ denotes the time step size. Using finite difference formulation combined with $\dot{\theta}$-weighted scheme, Eq. (1.1) can be discretized as [28]

$$\begin{aligned}&\frac{v(\zeta^*, t_{\mathrm{j+1}}^*) - v(\zeta^*, t_{\mathrm{j}}^*)}{\Delta t^*} + \dot{\theta}\left[\alpha\big(v(\zeta^*, t^*)v_{\zeta^*}(\zeta^*, t^*)\big)\right.\\ &\left.-\beta v(\zeta^*, t^*) + \beta v^2(\zeta^*, t^*) - f(\zeta^*, t^*)\right]^{\mathrm{j+1}}\\ &+(1-\dot{\theta})\left[\alpha\big(v(\zeta^*, t^*)v_{\zeta^*}(\zeta^*, t^*)\big) - \beta v(\zeta^*, t^*) + \beta\big(v^2(\zeta^*, t^*)\big) - f(\zeta^*, t^*)\right]^{\mathrm{j}}\\ &= 0, \quad \mathrm{j} = 0, 1, 2, \ldots \mathcal{J},\end{aligned} \tag{2.1}$$

where $0 \le \dot{\theta} \le 1$ and the indices j and $(\mathrm{j}+1)$ are successive time levels. Now, Rubin and Graves formula is used to linearize the nonlinear terms $\big(v(\zeta^*, t^*)v_{\zeta^*}(\zeta^*, t^*)\big)^{\mathrm{j+1}}$ and $\big(v^2(\zeta^*, t^*)\big)^{\mathrm{j+1}}$ [29]

$$\begin{cases}\big(v(\zeta^*, t^*)v_{\zeta^*}(\zeta^*, t^*)\big)^{\mathrm{j+1}} & = v(\zeta^*, t_{\mathrm{j+1}}^*)v_{\zeta^*}(\zeta^*, t_{\mathrm{j}}^*) + v(\zeta^*, t_{\mathrm{j}}^*)v_{\zeta^*}(\zeta^*, t_{\mathrm{j+1}}^*)\\ & \quad -v(\zeta^*, t_{\mathrm{j}}^*)v_{\zeta^*}(\zeta^*, t_{\mathrm{j}}^*),\\ \big(v^2(\zeta^*, t^*)\big)^{\mathrm{j+1}} & = 2v(\zeta^*, t_{\mathrm{j+1}}^*)v(\zeta^*, t_{\mathrm{j}}^*) - v(\zeta^*, t_{\mathrm{j}}^*)v(\zeta^*, t_{\mathrm{j}}^*).\end{cases} \tag{2.2}$$

Utilizing Eq. (2.2) into Eq. (2.1) results

$$\boldsymbol{\Phi}^{\mathrm{j}}v(\zeta^*, t_{\mathrm{j+1}}^*) + \boldsymbol{\Psi}^{\mathrm{j}}v_{\zeta^*}(\zeta^*, t_{\mathrm{j+1}}^*) = \boldsymbol{\Pi}^{\mathrm{j}}v(\zeta^*, t_{\mathrm{j}}^*) + F(\zeta^*, t_{\mathrm{j+1}}^*), \tag{2.3}$$

where

$$\boldsymbol{\Phi}^{\mathrm{j}} = \varpi + \alpha\dot{\theta}v_{\zeta^*}(\zeta^*, t_{\mathrm{j}}^*) - \dot{\theta}\beta + 2\beta\dot{\theta}v(\zeta^*, t_{\mathrm{j}}^*),$$

$$\boldsymbol{\Psi}^{\mathrm{j}} = \alpha\dot{\theta}v(\zeta^*, t_{\mathrm{j}}^*),$$

$$\boldsymbol{\Pi}^{\mathrm{j}} = \varpi + 2\alpha\dot{\theta}v_{\zeta^*}(\zeta^*, t_{\mathrm{j}}^*) - \alpha v_{\zeta^*}(\zeta^*, t_{\mathrm{j}}^*) + 2\beta\dot{\theta}v(\zeta^*, t_{\mathrm{j}}^*) - \beta v(\zeta^*, t_{\mathrm{j}}^*) + \beta(1-\dot{\theta}),$$

$$F(\zeta^*, t_{\mathrm{j+1}}^*) = \dot{\theta}f(\zeta^*, t_{\mathrm{j+1}}^*) + (1-\dot{\theta})f(\zeta^*, t_{\mathrm{j}}^*),$$

and

$$\varpi = \frac{1}{\Delta t^*}.$$

Eq. (2.3) is semi discretized form of the proposed problem.

2.2. Spatial discretization

Now, partition the spatial domain $[\dot{a}, \dot{b}]$ into $\mathcal{I}$ subintervals denoted by $[\zeta_i^*, \zeta_{i+1}^*]$, where $i = 0, 1, 2, \ldots, \mathcal{I}$. Here, $\zeta_i^* = \zeta_0^* + i\mathrm{h}$, where $\mathrm{h} = \frac{\dot{b}-\dot{a}}{\mathcal{I}}$ represents the size of each subinterval.

Let $\mathcal{V}(\zeta^*, t^*)$ be the extended cubic B-spline approximation that satisfies the prescribed conditions such that

$$\mathcal{V}(\zeta_i^*, t_{\mathrm{j+1}}^*) = \sum_{i=-1}^{\mathcal{I}+1}\delta_i(t_{\mathrm{j+1}}^*)\mathbb{E}_i(\zeta^*, \tilde{\lambda}), \tag{2.4}$$

where $\delta_i(t_{\mathrm{j+1}}^*)$ are time-dependent parameters, to be determined and $\mathbb{E}_i(\zeta^*, \tilde{\lambda})$ are four-degree basis spline functions [30], $\tilde{\lambda}$ is a free parameter which is used to change the shape of the B-spline curve and $-m(m-1) \le \tilde{\lambda} \le 1$, m is the degree of extended cubic B-spline functions. For $\tilde{\lambda} = 0$, the extended cubic B-spline functions reduce to ordinary cubic B-spline functions. The extended cubic B-spline functions can be expressed as follows

$$\mathbb{E}_i(\zeta^*, \tilde{\lambda}) = \frac{1}{24\mathrm{h}^4}\begin{cases}4\mathrm{h}(1-\tilde{\lambda})(\zeta^* - \zeta_{i-2}^*)^3 + 3\tilde{\lambda}(\zeta^* - \zeta_{i-2}^*)^4, & \zeta^* \in [\zeta_{i-2}^*, \zeta_{i-1}^*]\\ (4-\tilde{\lambda})\mathrm{h}^4 + 12\mathrm{h}^3(\zeta^* - \zeta_{i-1}^*) + 6\mathrm{h}^2(2+\tilde{\lambda})(\zeta^* - \zeta_{i-1}^*)^2 & \\ \quad -12\mathrm{h}(\zeta^* - \zeta_{i-1}^*)^3 - 3\tilde{\lambda}(\zeta^* - \zeta_{i-1}^*)^4, & \zeta^* \in [\zeta_{i-1}^*, \zeta_i^*]\\ (4-\tilde{\lambda})\mathrm{h}^4 - 12\mathrm{h}^3(\zeta^* - \zeta_{i+1}^*) + 6\mathrm{h}^2(2+\tilde{\lambda})(\zeta^* - \zeta_{i+1}^*)^2 & \\ \quad +12\mathrm{h}(\zeta^* - \zeta_{i+1}^*)^3 - 3\tilde{\lambda}(\zeta^* - \zeta_{i+1}^*)^4, & \zeta^* \in [\zeta_i^*, \zeta_{i+1}^*]\\ 4\mathrm{h}(\tilde{\lambda}-1)(\zeta^* - \zeta_{i+2}^*)^3 + 3\tilde{\lambda}(\zeta^* - \zeta_{i+2}^*)^4, & \zeta^* \in [\zeta_{i+1}^*, \zeta_{i+2}^*]\\ 0, & \text{otherwise.}\end{cases} \tag{2.5}$$

In terms of approximate solution, Eq. (2.3) can be written as

$$\begin{aligned}&\boldsymbol{\Phi}^{\mathrm{j}}\sum_{i=-1}^{\mathcal{I}+1}\delta_i(t_{\mathrm{j+1}}^*)\mathbb{E}_i(\zeta^*, \tilde{\lambda}) + \boldsymbol{\Psi}^{\mathrm{j}}\sum_{i=-1}^{\mathcal{I}+1}\delta_i(t_{\mathrm{j+1}}^*)\big(\mathbb{E}_i(\zeta^*, \tilde{\lambda})\big)_{\zeta^*}\\ &= \boldsymbol{\Pi}^{\mathrm{j}}\sum_{i=-1}^{\mathcal{I}+1}\delta_i(t_{\mathrm{j}}^*)\mathbb{E}_i(\zeta^*, \tilde{\lambda}) + F(\zeta^*, t_{\mathrm{j+1}}^*).\end{aligned} \tag{2.6}$$

Discretizing Eq. (2.6) along the spatial grid as follows

$$\begin{aligned}&\boldsymbol{\Phi}^{\mathrm{j}}\sum_{i=-1}^{\mathcal{I}+1}\delta_i(t_{\mathrm{j+1}}^*)\mathbb{E}_i(\zeta_i^*, \tilde{\lambda}) + \boldsymbol{\Psi}^{\mathrm{j}}\sum_{i=-1}^{\mathcal{I}+1}\delta_i(t_{\mathrm{j+1}}^*)\big(\mathbb{E}_i(\zeta_i^*, \tilde{\lambda})\big)_{\zeta^*}\\ &= \boldsymbol{\Pi}^{\mathrm{j}}\sum_{i=-1}^{\mathcal{I}+1}\delta_i(t_{\mathrm{j}}^*)\mathbb{E}_i(\zeta_i^*, \tilde{\lambda}) + F(\zeta_i^*, t_{\mathrm{j+1}}^*), \quad i = 0, 1, 2, \ldots, \mathcal{I}.\end{aligned} \tag{2.7}$$

From Eqs. (2.4) and (2.5), we obtain

$$\begin{cases}\sum_{i=-1}^{\mathcal{I}+1}\delta_i(t_{\mathrm{j+1}}^*)\mathbb{E}_i(\zeta_i^*, \tilde{\lambda}) & = \big(\frac{4-\tilde{\lambda}}{24}\big)\delta_{i-1}^{\mathrm{j+1}} + \big(\frac{16+2\tilde{\lambda}}{24}\big)\delta_i^{\mathrm{j+1}} + \big(\frac{4-\tilde{\lambda}}{24}\big)\delta_{i+1}^{\mathrm{j+1}},\\ \sum_{i=-1}^{\mathcal{I}+1}\delta_i(t_{\mathrm{j+1}}^*)\big(\mathbb{E}_i(\zeta_i^*, \tilde{\lambda})\big)_{\zeta^*} & = \big(\frac{-1}{2\mathrm{h}}\big)\delta_{i-1}^{\mathrm{j+1}} + \big(\frac{1}{2\mathrm{h}}\big)\delta_{i+1}^{\mathrm{j+1}}.\end{cases} \tag{2.8}$$

Substituting Eq. (2.8) into Eq. (2.7), we obtain the following set of equations

$$\mathfrak{p}_i^{\mathrm{j}}\delta_{i-1}^{\mathrm{j+1}} + \mathfrak{q}_i^{\mathrm{j}}\delta_i^{\mathrm{j+1}} + \mathfrak{r}_i^{\mathrm{j}}\delta_{i+1}^{\mathrm{j+1}} = \mathfrak{s}_i^{\mathrm{j}}, \quad i = 0, 1, 2, \ldots, \mathcal{I}, \quad \mathrm{j} = 0, 1, 2, \ldots, \mathcal{J}, \tag{2.9}$$

where

$$\mathfrak{p}_i^{\mathrm{j}} = \big(\frac{4-\tilde{\lambda}}{24}\big)\boldsymbol{\Phi}_i^{\mathrm{j}} - \frac{1}{2\mathrm{h}}\boldsymbol{\Psi}_i^{\mathrm{j}},$$

$$\mathfrak{q}_i^{\mathrm{j}} = \big(\frac{16+2\tilde{\lambda}}{24}\big)\boldsymbol{\Phi}_i^{\mathrm{j}},$$

$$\mathfrak{r}_i^{\mathrm{j}} = \big(\frac{4-\tilde{\lambda}}{24}\big)\boldsymbol{\Phi}_i^{\mathrm{j}} + \frac{1}{2\mathrm{h}}\boldsymbol{\Psi}_i^{\mathrm{j}},$$

and

$$\mathfrak{s}_i^{\mathrm{j}} = \boldsymbol{\Pi}_i^{\mathrm{j}}\sum_{i=-1}^{\mathcal{I}+1}\delta_i(t_{\mathrm{j}}^*)\mathbb{E}_i(\zeta_i^*, \tilde{\lambda}) + F(\zeta_i^*, t_{\mathrm{j+1}}^*).$$

The system (2.9) comprises a set of $(\mathcal{I}+1)$ equations involving $(\mathcal{I}+3)$ parameters of unknown values $\{\delta_{-1}^{\mathrm{j+1}}, \delta_0^{\mathrm{j+1}}, \delta_1^{\mathrm{j+1}}, \ldots, \delta_{\mathcal{I}+1}^{\mathrm{j+1}}\}$ at the time $t^{\mathrm{j+1}}$. In order to obtain a unique solution, two additional equations are required, which can be derived from the end conditions (1.3).

$$\begin{cases}\big(\frac{4-\tilde{\lambda}}{24}\big)\delta_{-1}^{\mathrm{j+1}} + \big(\frac{16+2\tilde{\lambda}}{24}\big)\delta_0^{\mathrm{j+1}} + \big(\frac{4-\tilde{\lambda}}{24}\big)\delta_1^{\mathrm{j+1}} & = \psi_1^{\mathrm{j+1}},\\ \big(\frac{4-\tilde{\lambda}}{24}\big)\delta_{\mathcal{I}-1}^{\mathrm{j+1}} + \big(\frac{16+2\tilde{\lambda}}{24}\big)\delta_{\mathcal{I}}^{\mathrm{j+1}} + \big(\frac{4-\tilde{\lambda}}{24}\big)\delta_{\mathcal{I}+1}^{\mathrm{j+1}} & = \psi_2^{\mathrm{j+1}}.\end{cases} \tag{2.10}$$

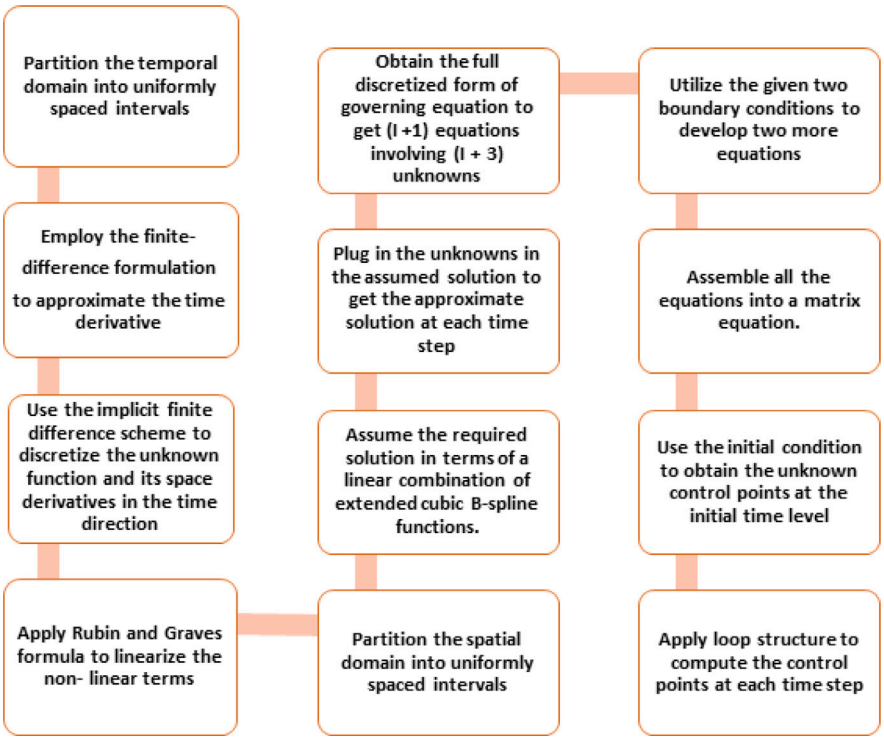

Fig. 1. Flowchart of numerical algorithm.

Eq. (2.9) combined with Eq. (2.10) can be expressed in a matrix form as

$$\begin{bmatrix} \frac{4-\tilde{\lambda}}{24} & \frac{16+2\tilde{\lambda}}{24} & \frac{4-\tilde{\lambda}}{24} & 0 & \cdots & 0 & 0 & 0 \\ \mathfrak{p}_0^{\mathrm{j}} & \mathfrak{q}_0^{\mathrm{j}} & \mathfrak{r}_0^{\mathrm{j}} & 0 & \cdots & 0 & 0 & 0 \\ 0 & \mathfrak{p}_1^{\mathrm{j}} & \mathfrak{q}_1^{\mathrm{j}} & \mathfrak{r}_1^{\mathrm{j}} & \cdots & 0 & 0 & 0 \\ \vdots & \vdots & \vdots & \vdots & \ddots & \vdots & \vdots & \vdots \\ 0 & 0 & 0 & 0 & \cdots & \mathfrak{p}_{\mathcal{I}}^{\mathrm{j}} & \mathfrak{q}_{\mathcal{I}}^{\mathrm{j}} & \mathfrak{r}_{\mathcal{I}}^{\mathrm{j}} \\ 0 & 0 & 0 & 0 & \cdots & \frac{4-\tilde{\lambda}}{24} & \frac{16+2\tilde{\lambda}}{24} & \frac{4-\tilde{\lambda}}{24} \end{bmatrix} \begin{bmatrix} \delta_{-1}^{\mathrm{j}+1} \\ \delta_0^{\mathrm{j}+1} \\ \delta_1^{\mathrm{j}+1} \\ \vdots \\ \delta_{\mathcal{I}}^{\mathrm{j}+1} \\ \delta_{\mathcal{I}+1}^{\mathrm{j}+1} \end{bmatrix} = \begin{bmatrix} (\psi_1)^{\mathrm{j}+1} \\ \mathfrak{s}_0^{\mathrm{j}+1} \\ \mathfrak{s}_1^{\mathrm{j}+1} \\ \vdots \\ \mathfrak{s}_{\mathcal{I}}^{\mathrm{j}+1} \\ (\psi_2)^{\mathrm{j}+1} \end{bmatrix}$$

The above system is solved for $[\delta_{-1}^{\mathrm{j}+1}, \delta_0^{\mathrm{j}+1}, \delta_1^{\mathrm{j}+1}, \ldots, \delta_{\mathcal{I}+1}^{\mathrm{j}+1}]^T$. Utilizing this vector in Eq. (2.4), the approximate solution at (j + 1)th time level for $\mathrm{j} = 1, 2, \ldots \mathcal{J} - 1$ can be obtained. However, initial vector $[\delta_{-1}^0, \delta_0^0, \delta_1^0, \ldots, \delta_{\mathcal{I}+1}^0]^T$ is needed to start the iterative process. The initial vector can be derived from the initial condition and boundary values of the derivatives of the initial condition as follows

$$\begin{cases} \mathcal{V}_{\zeta^*}(\zeta_0^*, t_0^*) &= \phi_{\zeta^*}(\zeta_0^*), \\ \mathcal{V}(\zeta_i^*, t_0^*) &= \phi(\zeta_i^*), \quad i = 0, 1, 2, \ldots, \mathcal{I}, \\ \mathcal{V}_{\zeta^*}(\zeta_{\mathcal{I}}^*, t_0^*) &= \phi_{\zeta^*}(\zeta_{\mathcal{I}}^*). \end{cases} \tag{2.11}$$

This results the following $(\mathcal{I}+3)\times(\mathcal{I}+3)$ matrix system

$$\begin{bmatrix} \frac{-1}{2\mathrm{h}} & 0 & \frac{1}{2\mathrm{h}} & 0 & \cdots & 0 & 0 & 0 \\ \frac{4-\tilde{\lambda}}{24} & \frac{16+2\tilde{\lambda}}{24} & \frac{4-\tilde{\lambda}}{24} & 0 & \cdots & 0 & 0 & 0 \\ \vdots & \vdots & \vdots & \vdots & \ddots & \vdots & \vdots & \vdots \\ 0 & 0 & 0 & 0 & \cdots & \frac{4-\tilde{\lambda}}{24} & \frac{16+2\tilde{\lambda}}{24} & \frac{4-\tilde{\lambda}}{24} \\ 0 & 0 & 0 & 0 & \cdots & \frac{-1}{2\mathrm{h}} & 0 & \frac{1}{2\mathrm{h}} \end{bmatrix} \begin{bmatrix} \delta_{-1}^0 \\ \delta_0^0 \\ \vdots \\ \delta_{\mathcal{I}}^0 \\ \delta_{\mathcal{I}+1}^0 \end{bmatrix} = \begin{bmatrix} (\phi_{\zeta^*})_0^0 \\ \phi_0^0 \\ \vdots \\ \phi_{\mathcal{I}}^0 \\ (\phi_{\zeta^*})_{\mathcal{I}}^0 \end{bmatrix}$$

The above matrix equation can be solved by Thomas algorithm. MATHEMATICA software has been used for numerical computations (see Fig. 1).

3. Stability

We will analyze the stability of presented scheme using the Von Neumann approach. We assume the homogeneous case of problem (1.1) by taking $f(\zeta^*, t^*) = 0$.

$$\frac{\partial v(\zeta^*, t^*)}{\partial t^*} + \alpha v(\zeta^*, t^*)\frac{\partial v(\zeta^*, t^*)}{\partial \zeta^*} - \beta v(\zeta^*, t^*)\big(1 - v(\zeta^*, t^*)\big) = 0. \tag{3.1}$$

Employing the method described in previous section for $\dot{\theta} = 1$ and considering the quantity v a locally constant d in the nonlinear terms, the fully discretized scheme for Eq. (3.1) becomes

$$\mathfrak{R}_1\delta_{i-1}^{\mathrm{j}+1} + \mathfrak{R}_2\delta_i^{\mathrm{j}+1} + \mathfrak{R}_3\delta_{i+1}^{\mathrm{j}+1} = \varpi\left(\frac{4-\tilde{\lambda}}{24}\right)\delta_{i-1}^{\mathrm{j}} + \varpi\left(\frac{16+2\tilde{\lambda}}{24}\right)\delta_i^{\mathrm{j}} + \varpi\left(\frac{4-\tilde{\lambda}}{24}\right)\delta_{i+1}^{\mathrm{j}}, \tag{3.2}$$

where

$$\mathfrak{R}_1 = \{\varpi + \beta(d-1)\}(\frac{4-\tilde{\lambda}}{24}) - \alpha\frac{d}{2\mathrm{h}},$$

$$\mathfrak{R}_2 = \{\varpi + \beta(d-1)\}(\frac{16+2\tilde{\lambda}}{24}),$$

$$\mathfrak{R}_3 = \{\varpi + \beta(d-1)\}(\frac{4-\tilde{\lambda}}{24}) + \alpha\frac{d}{2\mathrm{h}}.$$

Now, Fourier method will be used for stability analysis. The error at jth time stage is given by

$$\Lambda^{\mathrm{j}} = \mathfrak{n}^{\mathrm{j}} - \check{\mathfrak{n}}^{\mathrm{j}}, \tag{3.3}$$

where $\Lambda^{\mathrm{j}} = [\Lambda_1^{\mathrm{j}}, \Lambda_2^{\mathrm{j}}, \Lambda_3^{\mathrm{j}}, \ldots, \Lambda_{\mathcal{I}-1}^{\mathrm{j}}]^T$, is error vector, $\mathfrak{n}^{\mathrm{j}}$ represents the growth factor and $\check{\mathfrak{n}}^{\mathrm{j}}$ be its estimated value.

The Eq. (3.2) can be rewrite as

$$\mathfrak{R}_1\Lambda_{i-1}^{\mathrm{j}+1} + \mathfrak{R}_2\Lambda_i^{\mathrm{j}+1} + \mathfrak{R}_3\Lambda_{i+1}^{\mathrm{j}+1} = \varpi\left(\frac{4-\tilde{\lambda}}{24}\right)\Lambda_{i-1}^{\mathrm{j}} + \varpi\left(\frac{16+2\tilde{\lambda}}{24}\right)\Lambda_i^{\mathrm{j}} + \varpi\left(\frac{4-\tilde{\lambda}}{24}\right)\Lambda_{i+1}^{\mathrm{j}}. \tag{3.4}$$

Table 1
A comparison of exact and numerical solutions with absolute errors related to Example 5.1 when $t^* = 1$.

ζ^*	Exact solutions	[20]		Proposed method	
		Numerical solutions	Absolute errors	Numerical solutions	Absolute errors
0.1	2.45960	2.45060	4.64×10^{-2}	2.45960	7.82082×10^{-6}
0.2	2.22554	2.12740	8.14×10^{-3}	2.22554	5.38226×10^{-6}
0.3	2.01375	2.00638	7.37×10^{-3}	2.01375	3.11370×10^{-6}
0.4	1.82212	1.81545	6.67×10^{-3}	1.82212	1.09713×10^{-6}
0.5	1.64872	1.64269	6.03×10^{-3}	1.64872	9.12176×10^{-7}
0.6	1.49182	1.48636	5.46×10^{-3}	1.49182	4.89462×10^{-7}
0.7	1.34986	1.34492	4.94×10^{-3}	1.34986	3.95473×10^{-7}
0.8	1.22140	1.21693	4.47×10^{-3}	1.22140	2.97101×10^{-7}
0.9	1.10517	1.10113	4.04×10^{-3}	1.10517	1.98276×10^{-7}

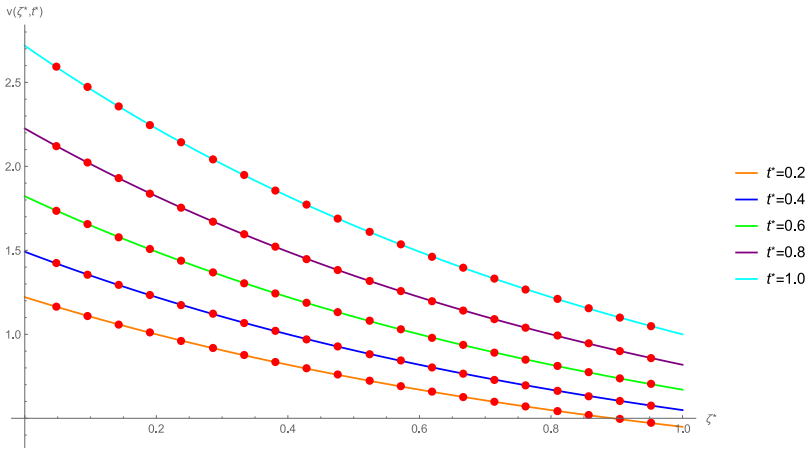

Fig. 2. Exact and computational solutions for Example 5.1 when $\mathcal{I} = 100$ and $\Delta t^* = 0.01$.

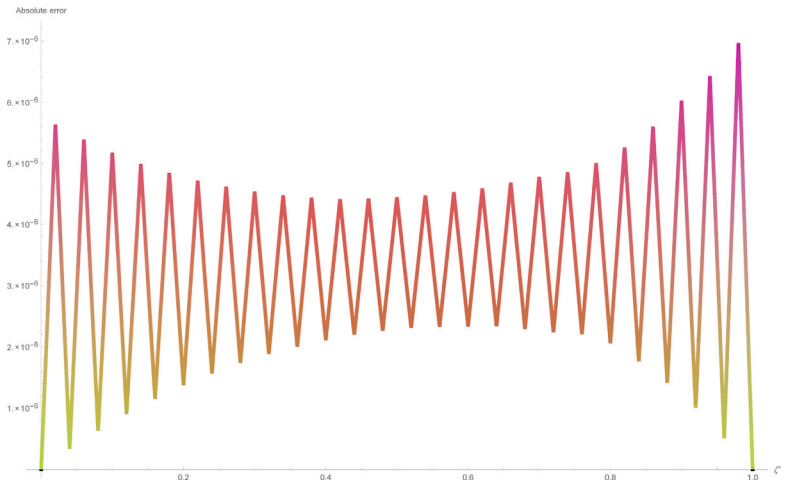

Fig. 3. A two-dimensional absolute error plot related to Example 5.1 for $\mathcal{I} = 50$, $\Delta t^* = 0.01$ and $t^* = 1$.

Table 2
L_∞ and L_2 error norms along temporal direction for Example 5.1.

Δt^*	$\mathcal{I} = 100$		$\mathcal{I} = 500$	
	L_∞	L_2	L_∞	L_2
0.008	2.68239×10^{-6}	1.42373×10^{-6}	1.08655×10^{-6}	4.90362×10^{-7}
0.004	1.80687×10^{-6}	9.28631×10^{-7}	2.97536×10^{-7}	1.34334×10^{-7}
0.002	5.75909×10^{-7}	2.93380×10^{-7}	9.94213×10^{-8}	4.54589×10^{-8}
0.0005	4.17536×10^{-8}	2.47868×10^{-8}	3.73519×10^{-8}	1.80030×10^{-8}

The error term are also satisfy the conditions (1.2)–(1.3) as follows

$$\Lambda_i^0 = \phi(\zeta_i^*), \quad \Lambda_0^{\mathrm{j}} = \psi_1(t_{\mathrm{j}}^*), \quad \Lambda_{\mathcal{I}}^{\mathrm{j}} = \psi_2(t_{\mathrm{j}}^*), \quad \mathrm{j} = 0, 1, \ldots, \mathcal{J}, \quad i = 1, 2, \ldots, \mathcal{I}. \tag{3.5}$$

Now introduce mesh function as follows

$$\Lambda^{\mathrm{j}} = \begin{cases} \Lambda_i^{\mathrm{j}}, & \zeta_i^* - \frac{\mathrm{h}}{2} \le \zeta^* \le \zeta_i^* + \frac{\mathrm{h}}{2}, \quad i = 1, 2, \ldots, \mathcal{I} - 1, \\ 0, & \dot{a} \le \zeta^* \le \dot{a} + \frac{\mathrm{h}}{2} \quad \text{or} \quad \dot{b} - \frac{\mathrm{h}}{2} \le \zeta^* \le \dot{b}. \end{cases} \tag{3.6}$$

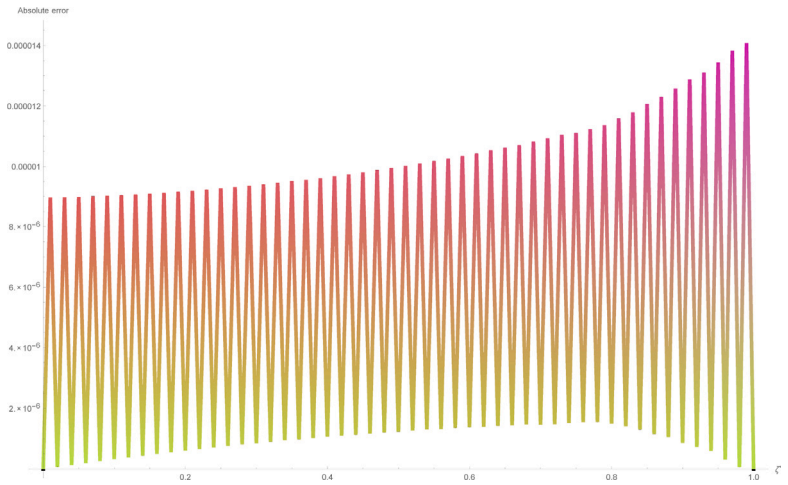

Fig. 4. A two-dimensional absolute error plot corresponding to Example 5.1 when $\mathcal{I} = 100$, $\Delta t^* = 0.01$ and $t^* = 1$.

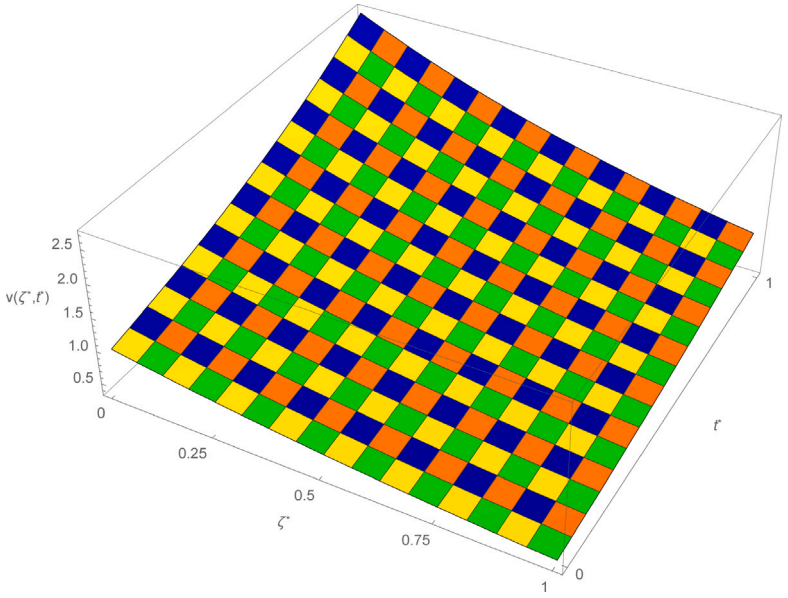

Fig. 5. A three-dimensional image showcasing the exact solutions for Example 5.1 when $\mathcal{I} = 100$, $\Delta t^* = 0.01$ and $t^* = 1$.

Table 3
Order of convergence and CPU time for Example 5.1 when $t^* = 1$ and $\Delta t^* = 0.001$.

h	L_∞	EOC	CPU time (s)
$\frac{1}{20}$	2.02689×10^{-4}		0.59375
$\frac{1}{40}$	5.10796×10^{-5}	1.98845	0.95312
$\frac{1}{80}$	1.27208×10^{-5}	2.00555	1.90625
$\frac{1}{160}$	3.06862×10^{-6}	2.05153	4.21880
$\frac{1}{320}$	6.45608×10^{-7}	2.08886	8.89100

Table 4
Error norms for Example 5.1 at various time knots when $\Delta t^* = 0.01$ and $\mathcal{I} = 200$.

t^*	L_∞	L_2
0.2	1.43846×10^{-5}	8.43859×10^{-6}
0.4	1.03478×10^{-5}	6.04358×10^{-6}
0.6	6.82588×10^{-6}	4.02859×10^{-6}
0.8	3.86713×10^{-6}	2.38254×10^{-6}
1.0	1.43559×10^{-6}	1.07070×10^{-6}

Then $\Lambda^{\mathrm{j}}(\zeta^*)$ can be expressed in the form of Fourier series as

$$\Lambda^{\mathrm{j}}(\zeta^*) = \sum_{-\infty}^{\infty} \pounds_{\mathrm{j}}(m) e^{\frac{2\pi \imath m \zeta^*}{\dot{b}-\dot{a}}}, \quad \mathrm{j} = 1, 2, \ldots, \mathcal{J}, \tag{3.7}$$

where

$$\pounds_{\mathrm{j}}(m) = \frac{1}{\dot{b}-\dot{a}} \int_{\dot{a}}^{\dot{b}} \Lambda^{\mathrm{j}}(\zeta^*) e^{\frac{-2\pi \imath m \zeta^*}{\dot{b}-\dot{a}}} d\zeta^*. \tag{3.8}$$

Table 5
Comparison of error norms when $\Delta t^* = 0.0001$, $\mathcal{I} = 40$ and $t^* = 0.1$ for Example 5.1.

	Crank–Nicolson [31]	Explicit [31]	Proposed method
L_∞	9.56570×10^{-6}	4.86090×10^{-6}	1.23314×10^{-10}
L_2	5.41720×10^{-6}	2.29400×10^{-6}	7.85713×10^{-11}

From the definition of norm

$$\|\Lambda^{\mathrm{j}}\|_2 = \sqrt{\sum_{i=1}^{\mathcal{I}-1} \mathrm{h} |\Lambda_i^{\mathrm{j}}|^2},$$

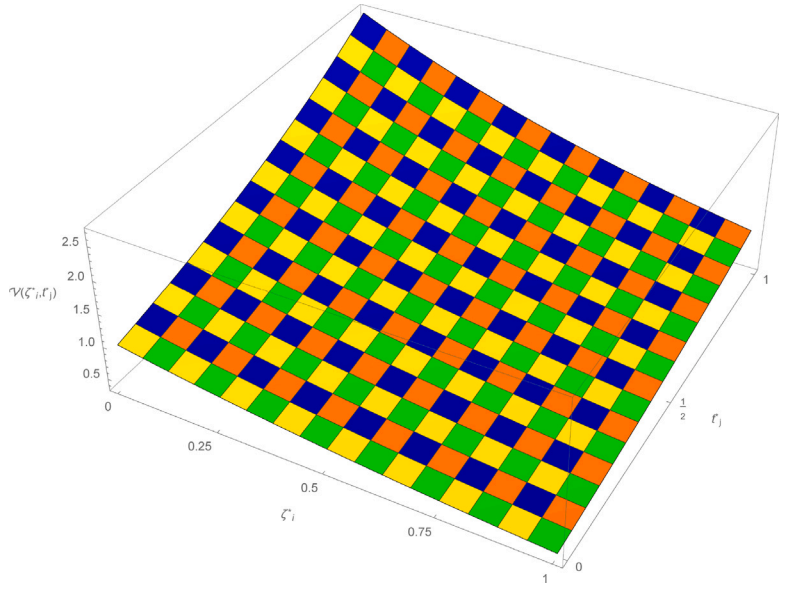

Fig. 6. A three-dimensional plot displaying the numerical outcomes for Example 5.1 when $\mathcal{I} = 100$, $\Delta t^* = 0.01$ and $t^* = 1$.

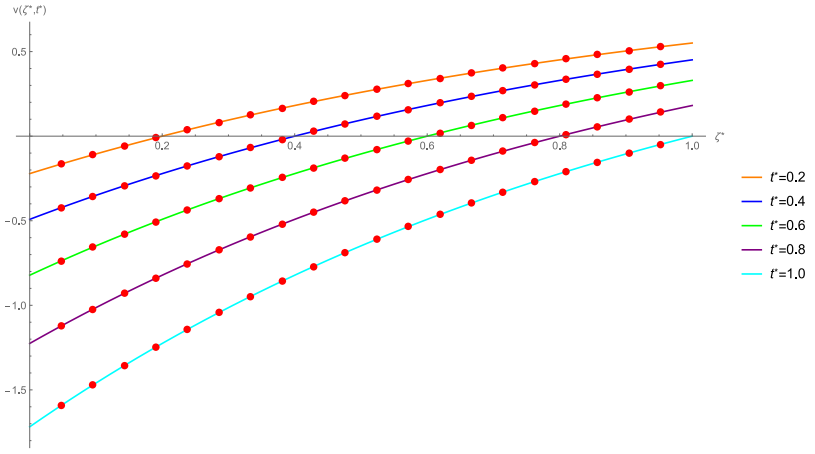

Fig. 7. Exact and numerical outcomes related to Example 5.2 for $\mathcal{I} = 100$ and $\Delta t^* = 0.01$ at different time knots.

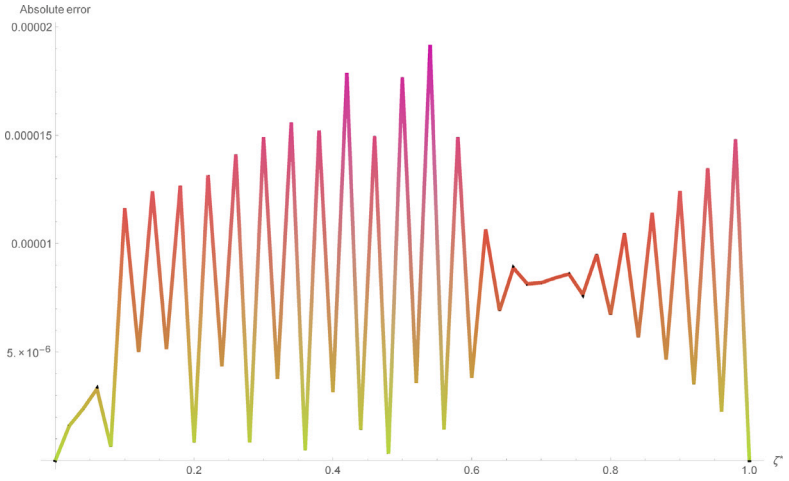

Fig. 8. A two-dimensional absolute error plot related to Example 5.2 when $\mathcal{I} = 50$, $\Delta t^* = 0.01$ and $t^* = 1$.

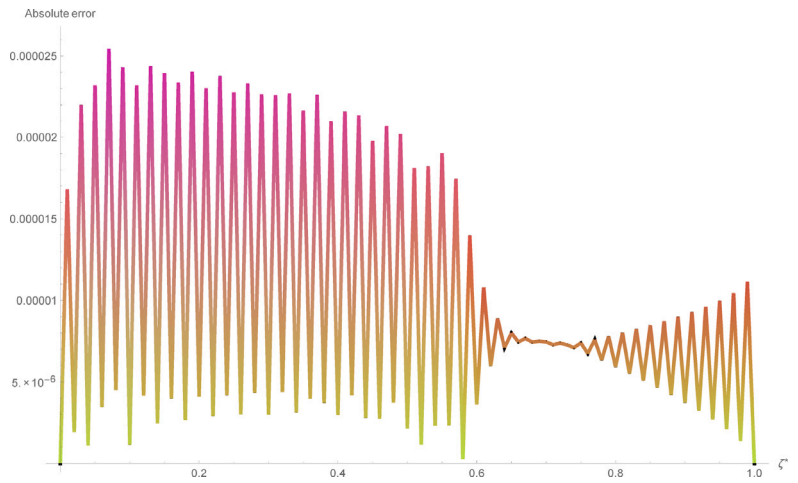

Fig. 9. A two-dimensional absolute error plot related to Example 5.2 when $\mathcal{I} = 100$, $\Delta t^* = 0.01$ and $t^* = 1$.

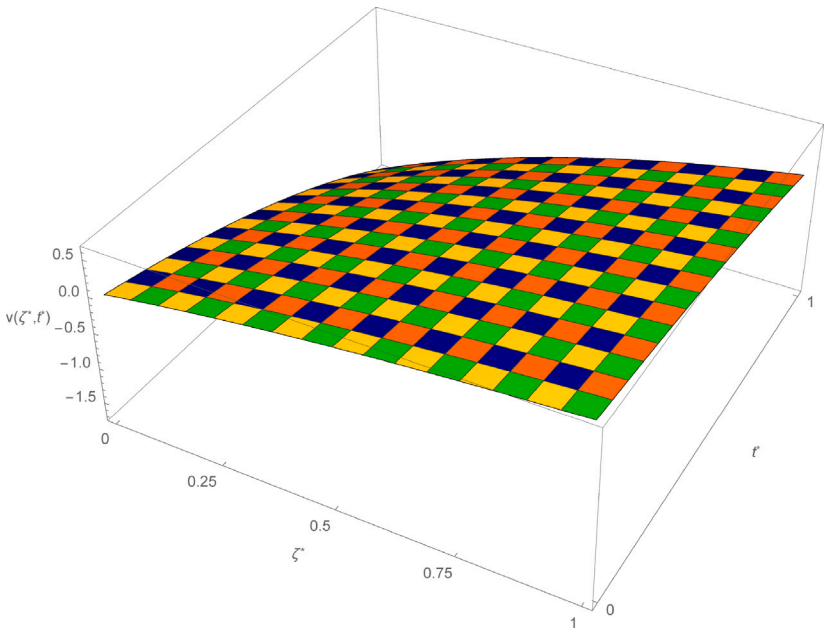

Fig. 10. A three-dimensional visualization of the exact solutions related to Example 5.2 when $\mathcal{I} = 100$, $\Delta t^* = 0.01$ and $t^* = 1$.

Table 6
Comparison of absolute errors with other studies for Example 5.2.

ζ^*	t^*	$\lvert v(\zeta^*,t^*) - \mathcal{V}_{RK-4}(\zeta^*,t^*)\rvert$	$\lvert v(\zeta^*,t^*) - \mathcal{V}(\zeta^*,t^*)\rvert$
		[6]	Proposed method
0.2	0.6	1.5×10^{-1}	3.24104×10^{-4}
0.4	0.7	2.1×10^{-1}	1.04583×10^{-4}
0.6	0.8	2.8×10^{-1}	4.40620×10^{-5}
0.8	0.9	3.3×10^{-1}	2.54870×10^{-5}
1	1	3.8×10^{-1}	0

Table 7
L_∞ and L_2 error norms along temporal direction for Example 5.2.

Δt^*	$\mathcal{I} = 100$		$\mathcal{I} = 500$	
	L_∞	L_2	L_∞	L_2
0.008	2.03088×10^{-5}	8.10899×10^{-6}	2.23629×10^{-6}	8.99559×10^{-7}
0.004	3.18215×10^{-6}	1.41284×10^{-6}	4.75725×10^{-7}	2.21660×10^{-7}
0.002	8.62342×10^{-7}	4.22866×10^{-7}	1.04776×10^{-7}	5.19355×10^{-8}
0.0005	4.98532×10^{-7}	9.65918×10^{-8}	2.08747×10^{-8}	4.95903×10^{-9}

$$= \sqrt{\int_{\dot{a}}^{\dot{a}+\frac{\hbar}{2}} |\Lambda^{\mathrm{j}}|^2 d\zeta^* + \sum_{i=1}^{\mathcal{I}-1} \int_{\zeta_i^*-\frac{\hbar}{2}}^{\zeta_i^*+\frac{\hbar}{2}} |\Lambda^{\mathrm{j}}|^2 d\zeta^* + \int_{\dot{b}-\frac{\hbar}{2}}^{\dot{b}} |\Lambda^{\mathrm{j}}|^2 d\zeta^*},$$

$$= \sqrt{\int_{\dot{a}}^{\dot{b}} |\Lambda^{\mathrm{j}}|^2 d\zeta^*}.$$

With the help of Parseval equality, we have

$$\int_{\dot{a}}^{\dot{b}} |\Lambda^{\mathrm{j}}|^2 d\zeta^* = \sum_{-\infty}^{\infty} |\pounds_{\mathrm{j}}(m)|^2,$$

which implies that

$$\|\Lambda^{\mathrm{j}}\|_2 = \sum_{-\infty}^{\infty} |\pounds_{\mathrm{j}}(m)|^2. \tag{3.9}$$

In the form of Fourier series analysis, the solution of Eqs. (3.4) and (3.5) can be described as

$$\Lambda_r^{\mathrm{j}} = \pi^{\mathrm{j}} e^{\iota \wp r \hbar}.$$

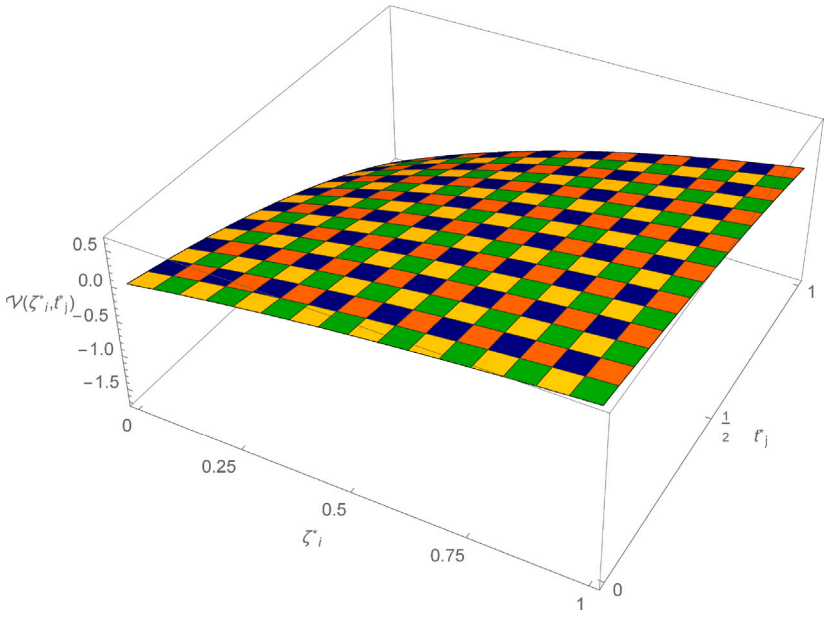

Fig. 11. A three-dimensional plot representing the numerical outcomes for Example 5.2 when $\mathcal{I} = 100$, $\Delta t^* = 0.01$ and $t^* = 1$.

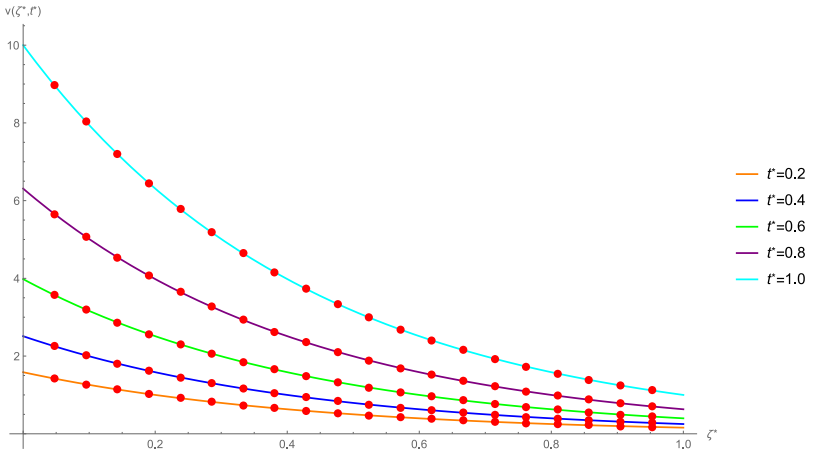

Fig. 12. The exact and computational outcomes for Example 5.3 when $\mathcal{I} = 100$ and $\Delta t^* = 0.01$ at various time knots.

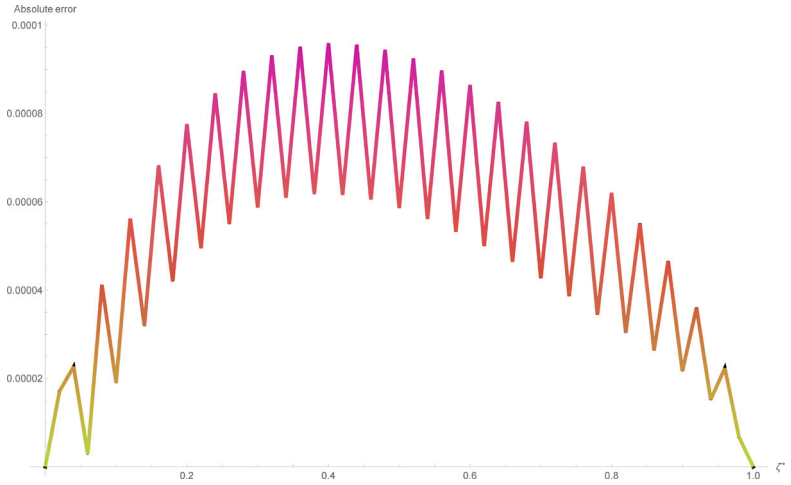

Fig. 13. A two-dimensional absolute error plot for Example 5.3 when $\mathcal{I} = 50$, $\Delta t^* = 0.01$ and $t^* = 1$.

Table 8
Order of convergence and CPU time for Example 5.2 when $t^* = 1$ and $\Delta t^* = 0.001$.

h	L_∞	EOC	CPU time (s)
$\frac{1}{20}$	2.63235×10^{-5}		0.07812
$\frac{1}{40}$	8.24532×10^{-6}	1.67470	0.20312
$\frac{1}{80}$	2.50283×10^{-6}	1.72002	0.50000
$\frac{1}{160}$	6.52481×10^{-7}	1.93955	1.04688
$\frac{1}{320}$	1.69949×10^{-9}	1.94083	2.09375

Table 9
Error norms at various time knots corresponding to Example 5.2 when $\Delta t^* = 0.01$ and $\mathcal{I} = 200$.

t^*	L_∞	L_2
0.2	2.95130×10^{-5}	1.38258×10^{-5}
0.4	1.08435×10^{-5}	8.97811×10^{-6}
0.6	6.45132×10^{-6}	5.50688×10^{-6}
0.8	9.52033×10^{-7}	6.03900×10^{-7}
1.0	4.61510×10^{-7}	1.30263×10^{-7}

Substituting the above expression in Eq. (3.4) and dividing by $e^{\iota \wp r \mathrm{h}}$, we get

$$\mathfrak{R}_1 \pi^{\mathrm{j}+1} e^{-\iota\wp \mathrm{h}} + \mathfrak{R}_2 \pi^{\mathrm{j}+1} + \mathfrak{R}_3 \pi^{\mathrm{j}+1} e^{\iota\wp \mathrm{h}} = \varpi\left(\frac{4-\tilde{\lambda}}{24}\right)\pi^{\mathrm{j}} e^{-\iota\wp \mathrm{h}} + \varpi\left(\frac{16+2\tilde{\lambda}}{24}\right)\pi^{\mathrm{j}} + \varpi\left(\frac{4-\tilde{\lambda}}{24}\right)\pi^{\mathrm{j}} e^{\iota\wp \mathrm{h}}, \tag{3.10}$$

where $\iota = \sqrt{-1}$ and $\wp = \frac{2\pi m}{b-a}$. After some simplifications and grouping like terms, Eq. (3.10) leads to

$$\pi^{\mathrm{j}+1} = \frac{1}{\chi}\pi^{\mathrm{j}}, \tag{3.11}$$

where $\chi = 1 + \frac{\beta(d-1)[(\frac{4-\tilde{\lambda}}{12})\cos\wp \mathrm{h} + \frac{16+2\tilde{\lambda}}{24}] + i\frac{\alpha d}{h}\sin\wp \mathrm{h}}{\varpi[(\frac{4-\tilde{\lambda}}{12})\cos\wp \mathrm{h} + \frac{16+2\tilde{\lambda}}{24}]}$.

Now, with the aid of mathematical induction, we have to show that $|\pi^{\mathrm{j}}| \le |\pi^0|$ for all j. For $\mathrm{j} = 0$, Eq. (3.11) gives

$$|\pi^1| = \frac{1}{\chi}|\pi^0| \le |\pi^0|, \quad \because \frac{1}{\chi} < 1. \tag{3.12}$$

Now, let us assume that $|\pi^{\mathrm{j}}| \le |\pi^0|$ for $\mathrm{j} = 0, 1, 2, \ldots \mathcal{J} - 1$. We have to prove it for $\mathrm{j} = p + 1$. Again from Eq. (3.11), we have

$$\begin{aligned} |\pi^{p+1}| &= |\frac{1}{\chi}\pi^p|, \\ &\le \frac{1}{\chi}|\pi^0|, \\ &\le |\pi^0|, \quad \because \frac{1}{\chi} < 1. \end{aligned}$$

Hence

$$|\pi^{p+1}| \le |\pi^0|. \tag{3.13}$$

From (3.9) and (3.13), we have

$$\|\Lambda^{\mathrm{j}}\|_2 \le \|\Lambda^0\|_2, \quad \text{for all } \mathrm{j}, \tag{3.14}$$

which results that the proposed scheme for nonlinear gas dynamics equation is unconditionally stable.

4. Convergence analysis

In this section, convergence of the cubic B-spline interpolation is examined that is based on Kadalbajoo and Arora's technique [32].

Theorem 4.1. *Let $v(\zeta^*, t^*)$ belongs to $C^4[\dot{a}, \dot{b}]$, f is in $C^2[\dot{a}, \dot{b}]$ and h be the length of evenly spaced partition of $[\dot{a}, \dot{b}]$. Let $\tilde{\mathcal{V}}(\zeta^*, t^*)$ be the unique spline approximation to the current problem at grid points $\{\zeta_0^*, \zeta_1^*, \ldots, \zeta_{\mathcal{I}}^*\}$, then $\exists$ μ_q free of h, such that*

$$\| D^q\big(v(\zeta^*, t^*) - \tilde{\mathcal{V}}(\zeta^*, t^*)\big)\|_\infty \le \mu_q \mathrm{h}^{4-q}, \quad q = 0, 1, 2. \tag{4.1}$$

Lemma 4.1. *The extended cubic B-spline basis functions $\{\mathbb{E}_{-1}, \mathbb{E}_0, \ldots, \mathbb{E}_{\mathcal{I}+1}\}$ presented in Eq. (2.5) hold the relation*

$$\sum_{i=-1}^{\mathcal{I}+1} |\mathbb{E}_i(\zeta^*, \tilde{\lambda})| \le \frac{7}{4}, \quad 0 \le \zeta^* \le 1. \tag{4.2}$$

Theorem 4.2. *Let $\mathcal{V}(\zeta^*, t^*)$ be the computational solution to the exact solution $v(\zeta^*, t^*)$ of Eqs. (1.1)–(1.3). In addition, if f belongs to $C^2[0, 1]$, we gain*

$$\|v(\zeta^*, t^*) - \mathcal{V}(\zeta^*, t^*)\|_\infty \le \aleph \mathrm{h}^2, \quad t^* \ge 0, \tag{4.3}$$

where $\aleph \ge 0$ is a constant not containing h and h is sufficiently small.

Proof. Let $\tilde{\mathcal{V}}(\zeta^*, t^*) = \sum_{i=0}^{\mathcal{I}+1} \tilde{\delta}_i \mathbb{E}_i$ be the approximated spline solution to the $\mathcal{V}(\zeta^*, t^*)$. Assume that the offered method achieve collocation restrictions

$$Lv(\zeta_i^*, t^*) = L\mathcal{V}(\zeta_i^*, t^*) = f(\zeta_i^*, t^*), \quad i = 0, 1, \ldots \mathcal{I},$$

then

$$L\tilde{\mathcal{V}}(\zeta_i^*, t^*) = \tilde{f}(\zeta_i^*, t^*), \quad i = 0, 1, \ldots \mathcal{I}.$$

At time level j, the above problem can be described in terms of difference equation as

$$\mathfrak{R}_1 \mathfrak{F}_{i-1}^{\mathrm{j}+1} + \mathfrak{R}_2 \mathfrak{F}_i^{\mathrm{j}+1} + \mathfrak{R}_3 \mathfrak{F}_{i+1}^{\mathrm{j}+1} = \varpi\left(\frac{4-\tilde{\lambda}}{24}\right)\mathfrak{F}_{i-1}^{\mathrm{j}} + \varpi\left(\frac{16+2\tilde{\lambda}}{24}\right)\mathfrak{F}_i^{\mathrm{j}} + \varpi\left(\frac{4-\tilde{\lambda}}{24}\right)\mathfrak{F}_{i+1}^{\mathrm{j}} + \big(\tilde{F}_i^{\mathrm{j}+1} - F_i^{\mathrm{j}+1}\big), \tag{4.4}$$

where $\mathfrak{F}_i^{\mathrm{j}} = \tilde{\delta}_i^{\mathrm{j}} - \delta_i^{\mathrm{j}}$, $i = 0, 1, \ldots, \mathcal{I}$, and boundaries are

$$\left(\frac{4-\tilde{\lambda}}{24}\right)\mathfrak{F}_{i-1}^{\mathrm{j}+1} + \left(\frac{16+2\tilde{\lambda}}{24}\right)\mathfrak{F}_i^{\mathrm{j}+1} + \left(\frac{4-\tilde{\lambda}}{24}\right)\mathfrak{F}_{i+1}^{\mathrm{j}+1} = 0, \quad i = 0, \mathcal{I}.$$

If $\Omega_i^{\mathrm{j}} = \mathrm{h}[\tilde{F}_i^{\mathrm{j}} - F_i^{\mathrm{j}}]$ for $i = 0, 1, \ldots, \mathcal{I}$, then using Theorem 4.1, we can write

$$|\Omega_i^{\mathrm{j}}| = \mathrm{h}|\tilde{F}_i^{\mathrm{j}} - F_i^{\mathrm{j}}| \le \mu_0 \mathrm{h}^4.$$

Let $\Omega^{\mathrm{j}} = \max\{|\Omega_i^{\mathrm{j}}|; 0 \le i \le \mathcal{I}\}$, $e_i^{\mathrm{j}} = |\mathfrak{F}_i^{\mathrm{j}}|$ and $e^{\mathrm{j}} = \max\{|\mathfrak{F}_i^{\mathrm{j}}|; 0 \le i \le \mathcal{I}\}$. The difference Eq. (4.4) for $\mathrm{j} = 0$ gives

$$\mathfrak{R}_1 e_{i-1}^1 + \mathfrak{R}_2 e_i^1 + \mathfrak{R}_3 e_{i+1}^1 = \varpi\left(\frac{4-\tilde{\lambda}}{24}\right)e_{i-1}^0 + \varpi\left(\frac{16+2\tilde{\lambda}}{24}\right)e_i^0 + \varpi\left(\frac{4-\tilde{\lambda}}{24}\right)e_{i+1}^0 + \frac{1}{\mathrm{h}}\Omega_i^1. \tag{4.5}$$

The initial condition suggests

$$e^0 = 0.$$

From Eq. (4.5), we get

$$\mathfrak{R}_2 e_i^1 = \frac{1}{\mathrm{h}}\Omega_i^1 - \mathfrak{R}_1 e_{i-1}^1 - \mathfrak{R}_3 e_{i+1}^1.$$

$$e_i^1 \le \mu_i^1 \mathrm{h}^2,$$

We obtain from the end conditions

$$e^1 \le \mu^1 \mathrm{h}^2, \tag{4.6}$$

where μ^1 is constant free of h. Mathematical induction can helps to easily show that

$$e_i^{r+1} \le \mu \mathrm{h}^2. \tag{4.7}$$

Hence

$$\tilde{\mathcal{V}}(\zeta^*, t^*) - \mathcal{V}(\zeta^*, t^*) = \sum_{i=-1}^{\mathcal{I}+1} \big(\tilde{\delta}_i(t^*) - \delta_i(t^*)\big)\mathbb{E}_i(\zeta^*, \tilde{\lambda}).$$

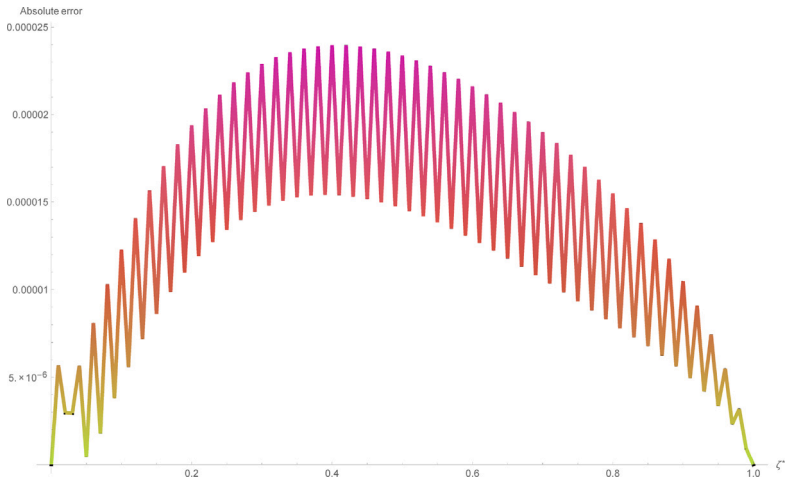

Fig. 14. A two-dimensional absolute error plot for Example 5.3 when $\mathcal{I} = 100$, $\Delta t^* = 0.01$ and $t^* = 1$.

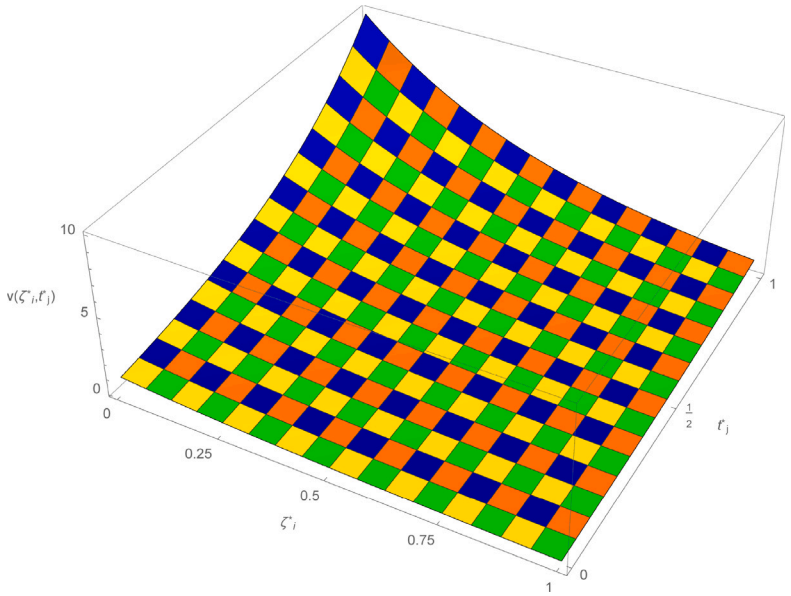

Fig. 15. A three-dimensional visualization of the exact outcomes for Example 5.3 when $\mathcal{I} = 100$, $\Delta t^* = 0.01$ and $t^* = 1$.

We achieve by Lemma 4.1

$$\|\tilde{\mathcal{V}} - \mathcal{V}\|_\infty \leq \frac{7}{4}\mu \mathrm{h}^2. \tag{4.8}$$

Using the triangular inequality, we have

$$\|v - \mathcal{V}\|_\infty \leq \|v - \tilde{\mathcal{V}}\|_\infty + \|\tilde{\mathcal{V}} - \mathcal{V}\|_\infty \leq \mu_0 \mathrm{h}^4 + \frac{7}{4}\mu \mathrm{h}^2 = \aleph \mathrm{h}^2,$$

where $\aleph = \mu_0 \mathrm{h}^2 + \frac{7}{4}\mu$, which presents second order convergence. □

5. Numerical evaluations

In this section, we provide numerical examples to showcase the application of the extended cubic B-spline approach. The accuracy of the proposed technique is evaluated by calculating the maximum error norms L_∞ and the Euclidean error norms L_2.

$$L_\infty = \|v - \mathcal{V}\|_\infty \simeq \max_{0 \leq i \leq \mathcal{I}} |v_i - \mathcal{V}_i|,$$

$$L_2 = \|v - \mathcal{V}\|_2 \simeq \sqrt{\mathrm{h} \sum_{i=0}^{\mathcal{I}} |v_i - \mathcal{V}_i|^2},$$

The experimental order of convergence (EOC) can be computed as

$$\mathrm{EOC} = \frac{\log(L_\infty(\mathcal{I})/L_\infty(2\mathcal{I}))}{\log(2)}.$$

Example 5.1. Consider the homogeneous nonlinear gas dynamics equation as follows [1]

$$\frac{\partial v}{\partial t^*} + v\frac{\partial v}{\partial \zeta^*} - v(1 - v) = 0, \tag{5.1}$$

subject to initial and boundary conditions

$$v(\zeta^*, 0) = e^{-\zeta^*}, \quad 0 \leq \zeta^* \leq 1,$$

$$v(0, t^*) = e^{t^*}, \quad v(1, t^*) = e^{-1+t^*}, \quad t^* > 0.$$

The exact solution to the problem is

$$v(\zeta^*, t^*) = e^{t^* - \zeta^*}.$$

Table 1 presents a comparison between exact solutions, numerical solutions, and absolute errors from the existing and the proposed method. The results demonstrate the efficiency of the proposed method compared to the existing approach. Table 2 provides the error norms computed along the temporal direction for different step sizes. Table

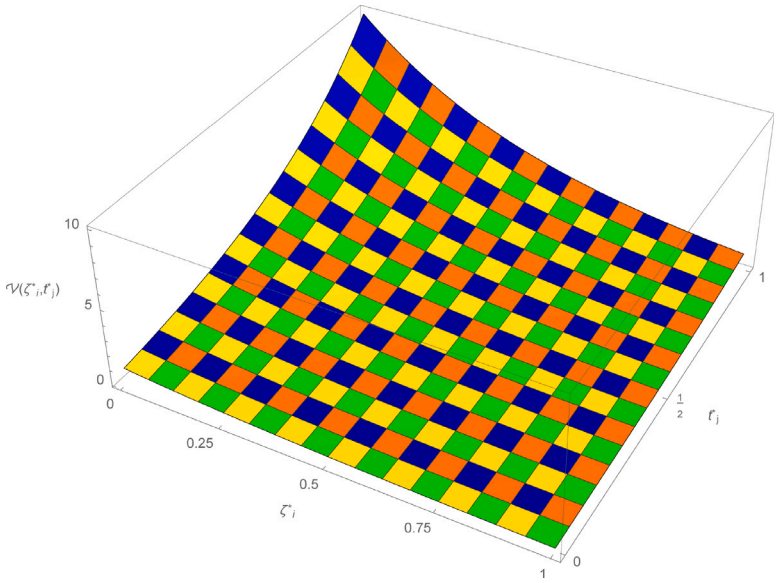

Fig. 16. A three-dimensional plot representing the numerical outcomes for Example 5.3 when $\mathcal{I} = 100$ and $\Delta t^* = 0.01$ and $t^* = 1$.

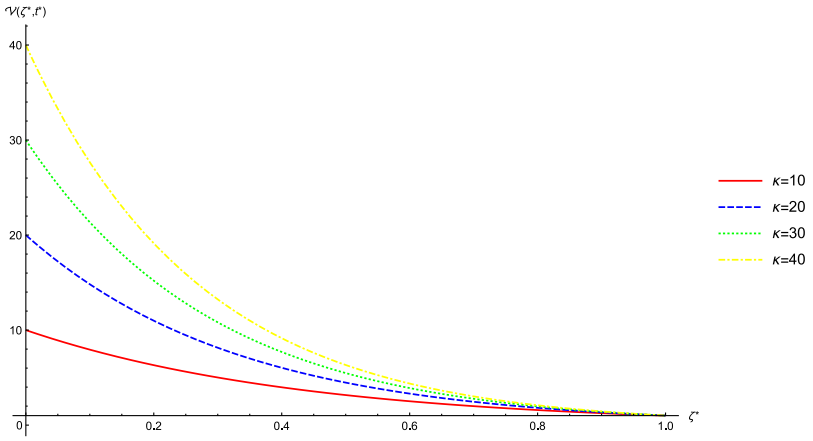

Fig. 17. The influence of κ on the computational solution for Example 5.3 when $\mathcal{I} = 100$, $\Delta t^* = 0.01$ and $t^* = 1$.

3 reports the numerical order of convergence along the corresponding calculation time in seconds. Table 4 offers a detailed comparison of error norms evaluated at various time knots. Table 5 highlights the improved error norms achieved by the proposed method compared to the explicit and Crank–Nicolson schemes. Fig. 2 depicts the computational and exact solutions at distinct time knots. Two-dimensional absolute error plots for different step sizes are displayed in Figs. 3 and 4. Figs. 5 and 6 present three-dimensional visualizations of the exact and numerical outcomes.

Example 5.2. Consider the nonhomogeneous nonlinear gas dynamics equation as follows [1]

$$\frac{\partial v}{\partial t^*} + v\frac{\partial v}{\partial \zeta^*} - v(1-v) = -e^{t^*-\zeta^*} \tag{5.2}$$

subject to initial and boundary conditions

$$v(\zeta^*, 0) = 1 - e^{-\zeta^*}, \quad 0 \le \zeta^* \le 1,$$

$$v(0, t^*) = 1 - e^{t^*}, \quad v(1, t^*) = 1 - e^{-1+t^*}, \quad t^* > 0.$$

The exact solution to the problem is

$$v(\zeta^*, t^*) = 1 - e^{t^*-\zeta^*}.$$

Table 6 provides a comparison of error norms between the Runge-Kutta-4 and the proposed method, highlighting the efficiency of the proposed approach across different time knots. Table 7 reports the error norms along the temporal direction for different step sizes, while Table 8 presents the numerical convergence order and the corresponding calculation time in seconds. Table 9 details the error norms computed at various time knots. Fig. 7 displays the exact and numerical outcomes at various time knots. Figs. 8 and 9 show two-dimensional error plots for different step sizes, whereas Figs. 10 and 11 depict the three-dimensional representations of the exact and numerical outcomes, respectively.

Example 5.3. Consider the homogeneous nonlinear gas dynamics equation as follows [9]

$$\frac{\partial v}{\partial t^*} + v\frac{\partial v}{\partial \zeta^*} - v(1-v)\log\kappa = 0, \quad \kappa > 0 \tag{5.3}$$

where κ is constant.

The initial and boundary conditions are

$$v(\zeta^*, 0) = \kappa^{-\zeta^*}, \quad 0 \le \zeta^* \le 1,$$

$$v(0, t^*) = \kappa^{t^*}, \quad v(1, t^*) = \kappa^{-1+t^*}, \quad t^* > 0.$$

Table 10
A comparison of exact and numerical solutions with absolute errors related to Example 5.3 for $\kappa = 10$ and $t^* = 1$.

ζ^*	Exact solutions	[9]		Proposed method	
		Numerical solutions	Absolute errors	Numerical solutions	Absolute errors
0.1	7.94328	7.92257	2.07033×10^{-2}	7.94327	4.21564×10^{-5}
0.2	6.30957	6.29312	1.64452×10^{-2}	6.30955	3.20797×10^{-5}
0.3	5.01187	4.99880	1.30629×10^{-2}	5.01184	2.04843×10^{-5}
0.4	3.98107	3.97069	1.03762×10^{-2}	3.98103	1.03678×10^{-5}
0.5	3.16227	3.15403	8.24215×10^{-3}	3.16224	9.78270×10^{-6}
0.6	2.51188	2.50533	6.54697×10^{-3}	2.51184	7.35903×10^{-6}
0.7	1.99526	1.99006	5.20044×10^{-3}	1.99522	6.35584×10^{-6}
0.8	1.58489	1.58076	4.13086×10^{-3}	1.58485	4.68335×10^{-6}
0.9	1.25892	1.25564	3.28125×10^{-3}	1.25889	3.59643×10^{-6}

Table 11
L_∞ and L_2 error norms along temporal direction for Example 5.3.

Δt^*	$\mathcal{I} = 100$		$\mathcal{I} = 500$	
	L_∞	L_2	L_∞	L_2
0.008	2.63129×10^{-6}	1.45363×10^{-6}	8.48233×10^{-7}	5.92035×10^{-7}
0.004	3.06281×10^{-7}	1.37599×10^{-7}	1.47155×10^{-7}	7.65537×10^{-8}
0.002	7.63017×10^{-8}	3.72048×10^{-8}	4.85724×10^{-8}	1.01789×10^{-8}
0.0005	1.68782×10^{-8}	6.84470×10^{-9}	5.16215×10^{-9}	1.22011×10^{-9}

Table 12
Order of convergence and CPU time for Example 5.3 when $t^* = 1$ and $\Delta t^* = 0.001$.

h	L_∞	EOC	CPU time (s)
$\frac{1}{10}$	8.42146×10^{-5}		0.40625
$\frac{1}{20}$	2.15667×10^{-5}	1.96527	0.78125
$\frac{1}{40}$	5.42025×10^{-6}	1.99237	1.60188
$\frac{1}{80}$	1.35248×10^{-6}	2.00274	3.20063
$\frac{1}{160}$	3.35325×10^{-7}	2.01198	6.85940

Table 13
Error norms computed at various time knots for Example 5.3 when $\Delta t^* = 0.01$ and $\mathcal{I} = 200$.

t^*	L_∞	L_2
0.2	5.26574×10^{-6}	2.90892×10^{-6}
0.4	3.77895×10^{-6}	2.11518×10^{-6}
0.6	2.46866×10^{-6}	1.44369×10^{-6}
0.8	8.77895×10^{-7}	6.11518×10^{-7}
1.0	1.20331×10^{-7}	9.14315×10^{-8}

The exact solution to the problem is

$$v(\zeta^*, t^*) = \kappa^{t^* - \zeta^*}.$$

Table 10 offers a comparative analysis between exact solutions, numerical solutions and absolute errors from the existing and the proposed method. The results highlight the efficiency of the proposed method compared to the existing approach. In Table 11, the error norms along the temporal direction computed for different step sizes are tabulated. Table 12 reports the numerical order of convergence along with the corresponding calculation time in seconds. Fig. 12 pictures the computational and exact solutions at distinct time knots. Two-dimensional absolute error plots for different step sizes are observed in Figs. 13 and 14. Figs. 15 and 16 provide three-dimensional visual representations of the exact and computational results. Additionally, the influence of κ on the computational solution is depicted in Fig. 17 (see Table 13).

Example 5.4. Consider the inhomogeneous nonlinear gas dynamics equation as follows [21]

$$\frac{\partial v}{\partial t^*} + v\frac{\partial v}{\partial \zeta^*} + (1 + t^*)^2 v^2 = \zeta^{*2}, \tag{5.4}$$

Table 14
A comparison of absolute errors for Example 5.4 when $t^* = 1$ with other studies.

ζ^*	[33]	[21]	Present method
0.2	5.68405×10^{-5}	3.46512×10^{-5}	3.89834×10^{-7}
0.4	4.65371×10^{-5}	3.21579×10^{-5}	2.33152×10^{-7}
0.6	3.81013×10^{-5}	2.34109×10^{-5}	1.54751×10^{-7}
0.8	3.11948×10^{-5}	2.41023×10^{-5}	1.33785×10^{-7}
1.0	2.52378×10^{-5}	1.03426×10^{-5}	6.06640×10^{-8}

Table 15
L_∞ and L_2 error norms along temporal direction for Example 5.4.

Δt^*	$\mathcal{I} = 100$		$\mathcal{I} = 500$	
	L_∞	L_2	L_∞	L_2
0.008	2.61150×10^{-6}	1.13777×10^{-6}	8.57630×10^{-7}	6.67595×10^{-7}
0.004	6.51272×10^{-7}	2.83747×10^{-7}	2.58329×10^{-7}	1.80835×10^{-7}
0.002	1.62619×10^{-7}	7.08501×10^{-8}	6.58680×10^{-8}	4.25112×10^{-8}
0.0005	1.01544×10^{-8}	4.42409×10^{-9}	2.58942×10^{-9}	1.2506×10^{-9}

Table 16
Order of convergence and CPU time for Example 5.4 when $t^* = 1$ and $\Delta t^* = 0.001$.

h	L_∞	EOC	CPU time (s)
$\frac{1}{10}$	3.33579×10^{-4}		0.17187
$\frac{1}{20}$	9.08550×10^{-5}	1.87639	0.29687
$\frac{1}{40}$	2.34299×10^{-5}	1.95521	0.73437
$\frac{1}{80}$	6.02078×10^{-6}	1.96033	1.50438
$\frac{1}{160}$	1.5007395×10^{-6}	2.00428	3.05625

subject to initial and boundary conditions

$$v(\zeta^*, 0) = \zeta^*, \quad 0 \le \zeta^* \le 1,$$

$$v(0, t^*) = 0, \quad v(1, t^*) = \frac{1}{1 + t^*}, \quad t^* > 0.$$

The exact solution to the problem is

$$v(\zeta^*, t^*) = \frac{\zeta^*}{1 + t^*}.$$

Table 14 provides a comprehensive comparison of absolute errors computed from the existing methods and proposed method. The results highlight the efficiency of the proposed method compared to the existing approach. Table 15 reports the error norms along the temporal direction for different step sizes. Table 16 presents the numerical convergence order and the corresponding calculation time in seconds. Table 17 details the error norms computed at various time knots. Fig. 18 displays the exact and numerical outcomes at various time knots. Figs. 19 and 20 depict the three-dimensional representations of the exact and numerical outcomes, respectively.

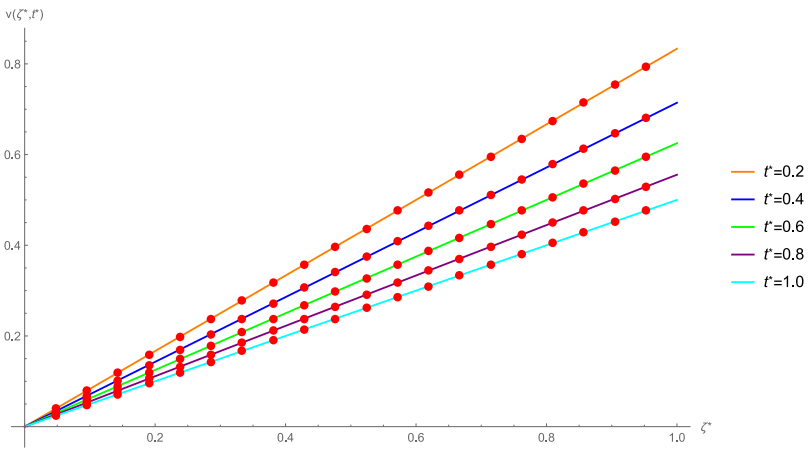

Fig. 18. The exact and computational solutions for Example 5.4 when $\mathcal{I} = 100$ and $\Delta t^* = 0.01$ at various time knots.

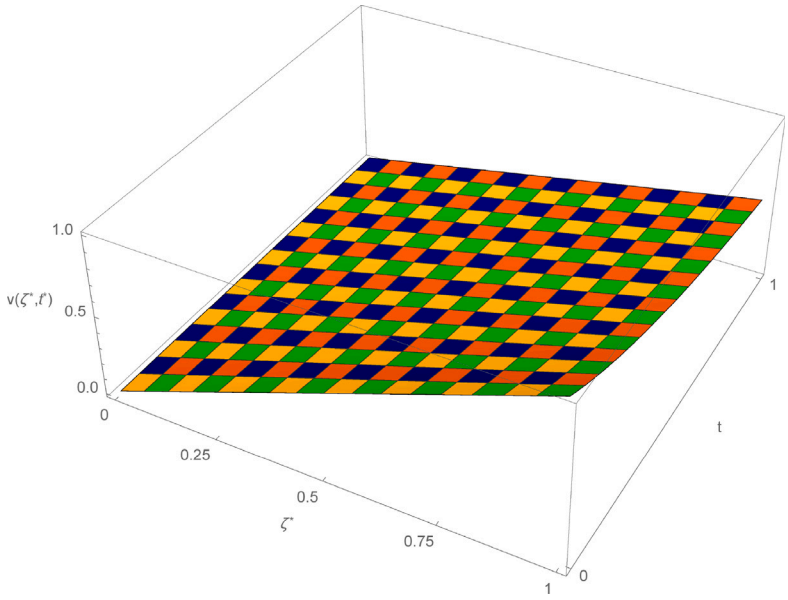

Fig. 19. A three-dimensional visualization of the exact solutions corresponding to Example 5.4 when $\mathcal{I} = 100$, $\Delta t^* = 0.01$ and $t^* = 1$.

Table 17
Error norms at various time knots corresponding to Example 5.4 when $\Delta t^* = 0.001$ and $\mathcal{I} = 200$.

t^*	L_∞	L_2
0.2	9.06300×10^{-5}	6.75824×10^{-5}
0.4	5.32506×10^{-5}	2.17580×10^{-5}
0.6	9.61982×10^{-6}	5.59262×10^{-6}
0.8	4.38758×10^{-6}	2.85483×10^{-6}
1.0	9.11979×10^{-7}	7.45365×10^{-7}

6. Conclusion

The authors conclude this work as

- A numerical approach based on extended cubic B-spline functions has been presented for the numerical simulation of the nonlinear gas dynamics equation.
- The typical finite difference formulation has been used to approximate the time derivative.
- The extended cubic B-spline functions have been used to interpolate the solution curve along the spatial direction.
- An unconditional bound for stability has been derived and convergence analysis for cubic B-spline interpolation is performed.
- To check the efficiency and accuracy of the presented scheme, the results of four numerical experiments with varying parameters have been examined.
- The experimental order of convergence is consistent with the theoretical results.
- The proposed method provides a spline function capable of approximating not only the unknown function but also its derivatives at any point within the interval, whereas the finite difference method yields the solution only at specific nodal points.
- The obtained computational results have been compared with both exact solutions and previously reported approximations in the literature. It is concluded that the presented approach provides more efficient results as compared to the existing methods.
- The proposed numerical method is simple, straightforward to implement, computationally efficient and shows superiority over traditional numerical approaches, making it a robust solution for nonlinear partial differential equations.

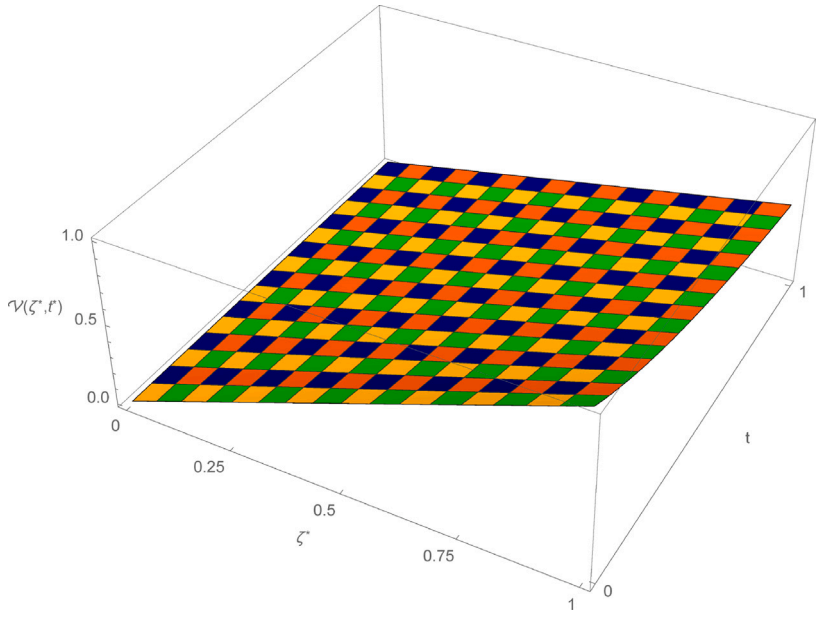

Fig. 20. A three-dimensional plot depicting the numerical outcomes for Example 5.4 when $\mathcal{I} = 100$, $\Delta t^* = 0.01$ and $t^* = 1$.

CRediT authorship contribution statement

Rabia Noureen: Writing – original draft, Methodology, Conceptualization, Software. **Muhammad Kashif Iqbal:** Validation, Conceptualization, Methodology, Writing – review & editing. **Maryam Asgir:** Methodology, Conceptualization, Software, Writing – original draft. **Bandar Almohsen:** Supervision, Resources, Conceptualization, Writing – review & editing, Formal analysis. **Muhammad Azeem:** Methodology, Validation, Conceptualization, Writing – original draft. **Husam A. Neamah:** Resources, Data curation, Writing – review & editing, Validation, Investigation.

Declaration of competing interest

The authors have no relevant financial or non-financial interests to disclose. We confirm that this work is original and has not been published elsewhere, nor is it currently under consideration for publication elsewhere.

Acknowledgments

Researchers Supporting Project number (RSP2023R158), King Saud University, Riyadh, Saudi Arabia.

Data availability

No data was used for the research described in the article.

References

[1] A.K. Adio, A reliable technique for solving gas dynamic equation using natural homotopy perturbation method, Acad. J. Appl. Math. Sci. 3 (8) (2017) 69–73.
[2] A.N. Golubyatnikov, D.V. Ukrainskii, On exact analytical solutions of gas dynamic equations, Fluid Dyn. 55 (3) (2020) 423–432.
[3] D.V. Ukrainskii, Exact solutions of gas dynamics equations in series in the Lagrangian coordinate and their numerical realization, Fluid Dyn. 55 (2020) 858–869.
[4] O.O. Olubanwo, A.T. Talabi, O.S. Odetunde, Z.O. Ogunwobi, Modified aboodh homotopy perturbation method for solving nonlinear gas dynamics equation, Lautech J. Eng. Technol. 13 (1) (2019) 1–12.
[5] I. Orynyak, I. Kostyushko, R. Mazuryk, Semi-analytical implicit direct time integration method for 1-D gas dynamic problem, Mech. Adv. Technol. 7 (1) (2023) (97).
[6] K. Dhirawat, R. Meher, Semi-analytical approach to nonlinear partial differential equations using homotopy analysis technique, Contemp. Math. 4 (4) (2023) 721–732.
[7] J.B. Yindoula, S.M. Mayembo, G. Bissanga, Application of Laplace variation iteration method to solving the nonlinear gas dynamics equation, Am. J. Math. Comput. Model. 5 (4) (2020) 127–133.
[8] S.O. Edeki, F.J. Adeyeye, G.O. Akinlabi, V.O. Udjor, Remarks on analytical solutions of a non-homogeneous gas dynamic model via successive approximation method, J. Phys.: Conf. Ser. 2199 (1) (2022) 012030.
[9] C. Kasumo, On analytical solutions of the classical gas dynamics equation, Int. J. Adv. Appl. Math. Mech. 10 (4) (2023) 1–7.
[10] W. Chen, Q. Yang, T. Diao, S. Ren, B-spline fusion line of sight algorithm for UAV path planning, Int. Conf. Guid. Navig. Control. 50 (2022) 3–512.
[11] G. Rousseau, C.S. Maniu, S. Tebbani, M. Babel, N. Martin, Minimum-time B-spline trajectories with corridor constraints. Application to cinematographic quadrotor flight plans, Control Eng. Pract. 89 (2019) 190–203.
[12] N.T. Nguyen, L. Schilling, M.S. Angern, H. Hamann, F. Ernst, G. Schildbach, B-spline path planner for safe navigation of mobile robots, Int. Conf. Intell. Robot. Syst. 33 (2021) 9–345.
[13] K. Wang, B-splines joint trajectory planning, Comput. Ind. 10 (2) (1988) 113–122.
[14] R. Van Hoek, J. Ploeg, H. Nijmeijer, Cooperative driving of automated vehicles using B-splines for trajectory planning, Trans. Intell. Veh. 6 (3) (2021) 594–604.
[15] H. Ali, N. Senu, Direct solution of third-order linear integro-differential equation using cubic B-spline method, J. Qual. Meas. Anal. 21 (1) (2025) 113–132.
[16] M. Iqbal, N. Zainuddin, H. Daud, R. Kanan, H. Soomro, R. Jusoh, A. Ullah, I.K. Khan, A modified basis of cubic B-spline with free parameter for linear second order boundary value problems: Application to engineering problems, J. King Saud Univ.-Sci. 36 (9) (2024) 103397.
[17] A. Yousafzai, S. Haq, A. Ghafoor, K. Shah, T. Abdeljawad, Solution of the foam-drainage equation with cubic B-spline hybrid approach, Phys. Scr. 99 (7) (2024) 075279.
[18] B. Latif, S.A. Abdul Karim, I. Hashim, New cubic B-spline approximation for solving linear two-point boundary-value problems, Mathematics 9 (11) (2021) 1250.
[19] A. Prakash, M. Kumar, Numerical method for time-fractional Gas dynamic equations, Proc. Natl. Acad. Sci. India Sect. A: Phys. Sci. 89 (2019) 559–570.
[20] M. Nadeem, M.M. Ali, Analytical and approximate solutions of the nonlinear gas dynamic equation using a hybrid approach, J. Math. Univ. Tokushima 2023 (1) (2023) 3136490.
[21] A. Akgul, A. Cordero, J.R. Torregrosa, Solutions of fractional gas dynamics equation by a new technique, Math. Methods Appl. Sci. 43 (3) (2020) 1349–1358.
[22] F. Iyanda, Algorithm analytic-numeric solution for nonlinear gas dynamic partial differential equation, Eng. Appl. Sci. Lett. 5 (2022) 32–40.
[23] H. Bin Jebreen, C. Cattani, Solving fractional gas dynamics equation using Müntz–Legendre polynomials, Symmetry 15 (11) (2023) 2076.
[24] M.A. Yousif, J.L. Guirao, P.O. Mohammed, N. Chorfi, D. Baleanu, A computational study of time-fractional gas dynamics models by means of conformable finite difference method, AIMS Math. 9 (7) (2024) 19843–19858.

[25] R. Noureen, M.N. Naeem, D. Baleanu, P.O. Mohammed, M.Y. Almusawa, Application of trigonometric B-spline functions for solving Caputo time fractional gas dynamics equation, AIMS Math. 8 (2023) 25343–25370.
[26] R. Noureen, M.K. Iqbal, M. Asgir, B. Almohsen, M. Azeem, A novel approach to approximate solution of time fractional gas dynamics equation with Atangana–Baleanu derivative, Alex. Eng. J. 116 (2025) 451–471.
[27] R. Noureen, M. Asgir, M.K. Iqbal, M. Azeem, Approximate solution of time-fractional gas dynamics equation using exponential B-spline functions, Opt. Quantum Electron. 57 (3) (2025) 197.
[28] M. Amin, M. Abbas, M.K. Iqbal, D. Baleanu, Numerical treatment of time-fractional Klein–Gordon equation using redefined extended cubic B-spline functions, Front. Phys. 8 (288) (2020).
[29] S.G. Rubin, R.A. Graves Jr., Viscous flow solutions with a cubic spline approximation, Comput. & Fluids 3 (1) (1975) 1–36.
[30] M. Amin, M. Abbas, D. Baleanu, M.K. Iqbal, M.B. Riaz, Redefined extended cubic B-spline functions for numerical solution of time-fractional telegraph equation, Comput. Model. Eng. Sci. 127 (1) (2021) 361–384.
[31] A. Esen, B. Karaagac, O. Tasbozan, Finite difference methods for fractional gas dynamics equation, Appl. Math. Inf. Sci. Lett. 4 (1) (2016) 1–4.
[32] M.K. Kadalbajoo, P. Arora, B-spline collocation method for the singular-perturbation problem using artificial viscosity, Comput. Math. Appl. 57 (4) (2009) 650–663.
[33] J. Singh, D. Kumar, A. Kılıçman, Homotopy perturbation method for fractional gas dynamics equation using Sumudu transform, Abstr. Appl. Anal. 2013 (1) (2013) 934060.